3-2021

Development of a Testbed for Foot Mounted based Pedestrian Dead Reckoning (PDR) systems

Jordan E. Eldridge

DEVELOPMENT OF A TESTBED FOR FOOT MOUNTED BASED PEDESTRIAN DEAD RECKONING(PDR) SYSTEMS

THESIS

Jordan E. Eldridge, Captain, USAF

AFIT-ENG-MS-21-M-032

DEPARTMENT OF THE AIR FORCE
AIR UNIVERSITY

AIR FORCE INSTITUTE OF TECHNOLOGY

Wright-Patterson Air Force Base, Ohio

AFIT-ENG-MS-21-M-032

DEVELOPMENT OF A TESTBED FOR FOOT MOUNTED BASED PEDESTRIAN DEAD RECKONING SYSTEMS

THESIS

Presented to the Faculty

Department of Electrical and Computer Engineering

Graduate School of Engineering and Management

Air Force Institute of Technology

Air University

Air Education and Training Command

in Partial Fulfillment of the Requirements for the

Degree of Master of Science in Electrical Engineering

Jordan E. Eldridge, B.S.E.E.

Captain, USAF

March 26, 2020

AFIT-ENG-MS-21-M-032

DEVELOPMENT OF A TESTBED FOR FOOT MOUNTED BASED PEDESTRIAN DEAD RECKONING SYSTEMS

THESIS

Jordan E. Eldridge, B.S.E.E.
Captain, USAF

Committee Membership:

Clark Taylor, Ph.D
Chair

Major Joseph Curro, Ph.D
Member

David Woodburn, Ph.D
Member

AFIT-ENG-MS-21-M-032

Abstract

The world has had an increasing reliance on the use of navigational aids. Even with these aids, most of us probably had experiences of having some difficulty pinpointing our exact location in sub-optimal conditions, such as when you are walking through a building or the woods. One solution to this problem is to utilize a Pedestrian Dead Reckoning (PDR) system that enables standalone personal tracking. Over the last several years of research into the field of PDR, there have been varying degrees of success in providing a viable individual navigation system.

While there is a variety of potential solutions, this thesis identifies the beginning of a testing environment for wearable PDR systems. Research accomplished by Laverne et al. (2019) verifies that by utilizing a micro-mechanical Inertial Measurement Unit (IMU) on each foot (along with the application of Zero Velocity Update (ZUPT)s and foot-to-foot range measurements) a reliable method of PDR tracking could be accomplished. Laverne's research utilized large, heavy, and expensive high-grade micro-mechanical IMUs along with a complex RF-based system to provide accurate results. Their study concludes that further evaluation is required for this foot-mounted solution to be viable as a wearable PDR system.

This thesis sets out to develop a testbed for foot-based PDR systems enabling AFIT to evaluate various sensors and techniques. In order to assess the PDR testbed, three PDR systems were implemented and evaluated. The first is a single foot-mounted IMU system with ZUPTs. The second is a dual foot-mounted IMU system with ZUPTs. The third is a dual foot-mounted IMU system with ZUPTs and a relative position magnetic sensor for foot-to-foot ranging measurements. This research is conducted primarily through the post-processing of real-world data utilizing

the Scorpion Development Toolkit (STK). This real-world data used to evaluate the three PDR systems are collected by walking laps around a standard track or walking around residential neighborhoods, using a custom-designed wearable device. The same data sets and step detection algorithms are utilized to compare the PDR systems implemented. The evaluation of the systems is accomplished by comparing the results against a "ground truth" provided by a Global Navigation Satellite System (GNSS).

To my Wife, Mom, Dad, and Brother.

Thank you for your tireless support

Table of Contents

Page

List of Figures

Figure Page

List of Tables

DEVELOPMENT OF A TESTBED FOR FOOT MOUNTED BASED PEDESTRIAN DEAD RECKONING SYSTEMS

I. Introduction

1.1 Motivation

We have all become accustomed to having the ability to navigating from any given point to another with high levels of accuracy. The world has had an increasing reliance on navigation that substantially relies on using the Global Positioning System (GPS). When you are walking through a park or trying to navigate yourself to some location, the positional accuracy given by GPS is excellent. This is because when outside and in optimal conditions, GPS currently provides an unmatched level of accuracy in the realm of position, Navigation, and timing.[3]

However, most of us have probably had the experience of trying to use their phone to navigate through a building, finding their location on a hiking trail, or even on a walk through a city and had difficulties identifying our exact location. Dead Reckoning, or navigation via inertial sensors, is a potential solution for navigating through these types of environments. Pedestrian Dead Reckoning (PDR) takes the concept of Dead Reckoning and employs those concepts in novel ways to suit human motion's nuances better. PDR is the method of identifying an individual's location based on a known starting point and combining the mechanization of inertial sensors such as accelerometers, gyroscopes, and magnetometers. By mechanizing the IMU, gyroscopes and accelerometers can be used to track a person's heading and detect their steps and movements, respectively. [4]. PDR generally involves wearing additional

sensors on the body in various fashions into a standalone personal tracking system such that a navigation solution is formed.

While there have been several years of research into the field of PDR, there have been varying degrees of success in providing a personal navigation system. Sections 2.7.1 and 2.7.2 briefly outlines some of the other PDR solutions however, this thesis focuses particularly on the research done by [5, 6]. Through their research, they identify that by utilizing a micro-mechanical IMU on each foot along with the application of Zero Velocity Update (ZUPT)s and foot-to-foot range measurements, a reliable method of PDR tracking could be accomplished.

The ZUPTs is a method which [7] describes as a crucial role in land-based navigation and is an effective technique for reducing and correcting errors in high precision systems. This is accomplished by identifying the intervals in which a system is stopped, and an update can be applied to compensate for any movements detected in the system. Through the research in [5, 6] the ZUPT is applied during each of the footfalls that are detected using a step detection algorithm. This ZUPT technique enabled a reduction in the sensor error, predominantly in the cross-range axis, improving the personal navigation system.

As stated earlier, in addition to the ZUPT [5, 6] utilized a foot-to-foot ranging measurement. This measurement is provided by a detector at the waist measures phase change, measuring the distance between the two feet. This is accomplished using a bulky frequency generator at the waist and a system of RF transmitters/receivers mounted to each foot to create a closed-loop RF system. Their research states that the addition of the foot-to-foot ranging measurement can further reduce the position error by an additional two orders of magnitude.

Brand and Phillips in [5] concludes that there is a trade-off to getting this level of accuracy in the overall Size, Weight, and Power (SWaP) of the system. That

trade-off comes in the form of expensive micro-mechanical Inertial Measurement Unit (IMU)s and a large and heavy RF system that has to be carried and mounted to the user's boots. Their recommended solution to mitigate this burden is integrating these sensors into clothing. Which a testbed would be the ideal solution for developing and assessing other PDR techniques as well as other sensors to provide a viable wearable PDR solution

1.2 Applications

PDR provides more than just the convenience of being able to navigate a hiking path with high accuracy until a time where GPS is more readily available. PDR can have the potential to increase a first responders' situational awareness in events such as traversing through a multi-story apartment building or providing search and rescue during a natural disaster. [8, 6] Other potential use cases outlined by [6] include enabling businesses to provide a mapping of products for their customers in the store or providing some form of additional, or augmented guidance, for individuals that are visually impaired.

1.3 Objective

This thesis's overall purpose is to develop a testbed for foot-based PDR systems to enable the Air Force Institute of Technology (AFIT) to evaluate various sensors and techniques. As stated earlier, the research done by [5, 6] is one particular solution to developing a PDR solution and is the basis of this research. Recall that to achieve a high level of precision [5, 6] used cumbersome but very precise high quality micro-mechanical IMUs and an extensive RF-based ranging system for the foot-to-foot measurements. They concluded that more analysis of integration methods would be required to provide a viable approach.

The PDR systems by replacing the micro-mechanical IMUs with lower-cost commercial IMUs. It will also attempt to assess the replacement of the large RF-based foot-to-foot range measurements with smaller relative pose magnetic sensors. This objective will be accomplished through an iterative development process. An overview of how this thesis will meet these objectives is described in the following section.

1.4 Methodology Overview

This research is conducted through the post-processing of real-world data utilizing the Scorpion software toolkit. To assess if the PDR "testbed" is successful, three separate PDR solutions are designed. The first is a single and Dual IMU PDR which utilized a ZUPT algorithm, commercial-grade IMU. The process starts by ensuring the step detection algorithm accurately identifies the steps taken for the ZUPT. The second PDR solution is a Dual IMU PDR systems that utilized a pair of commercial-grade IMUs and the same ZUPT algorithm as the first system. Lastly, the third system built upon the second with the addition of magnetic sensors that provided a foot-to-foot ranging measurement to the dual IMU PDR solution.

These data sets used to evaluate the different PDR iterations will be collected by either walking laps around a standard track or through residential neighborhoods utilizing a custom-designed wearable system. To evaluate the errors of each approach, the "ground truth" will be computed using a Global Navigation Satellite System (GNSS)/IMU fused solution. A comparison is made for each of the previously outlined systems, comparing the overall trajectories with the truth data collected.

1.5 Document Overview

This document is organized as follows. Chapter II consists of two sections, with the first providing a mathematical overview of some of the relevant background in-

formation required to understand the research done. The second section provides a brief synopsis of some of the related PDR research previously accomplished. Chapter III provides an overview of how the research is tested, including descriptions of the equipment and software used and how the equipment is configured. This chapter also provides the process of development and implementation for the single IMU and Dual IMU PDR algorithms. Chapter IV presents the results of evaluating variations in the two PDR algorithms. Finally, Chapter V summarizes and presents the overall conclusions drawn from the research results. This final chapter also identifies some areas of future research that can provide improvements to the PDR done in this thesis.

II. Background

2.1 Overview

The purpose of this chapter is to provide a brief background of the underlying theories, conventions and techniques used in this research. This chapter consists of the following sections:

- An overview of the frames of reference used for navigation.
- A description of the function and usage of accelerometers and gyroscopes as well as a derivation of the navigation equations utilized.
- A breakdown of how the Kalman Filter (KF) is setup and utilized, as well as, how to implement an Extended Kalman Filter (EKF).
- A brief background of the Pedestrian Dead Reckoning (PDR) systems that have been designed by other researchers.

2.2 Coordinate and Reference Frames

In order to navigate effectively around Earth using strapdown inertial navigation there are a set of defined coordinate that must be understood and pre-defined[9]. These reference frames enable a relationship to be precisely defined between the inertial measurements and the position over time of the inertial sensor on the earth. In this thesis, each reference frame that is utilized and outlined below is defined using an orthogonal, right-handed set of axes. This section follows the work and descriptions outlined throughout [9, 10] and [11].

2.2.1 Inertial Frame

The Earth-centered inertial frame or i-frame is a reference frame that is fixed and therefore with respect to the stars considered a non-rotating frame. The i-frame has its origin at the center of the Earth. The vertical or z-axis is aligned with World Geodetic System of 1984 (WGS-84) definition of the North Pole to account for the drift of the North pole while the Horizontal axis aligned with the equatorial plane.

2.2.2 Earth Frame

The Earth-centered Earth-fixed frame, or e-frame, like the i-frame, is a reference frame that has its origin at the center of the earth and uses the WGS-84 system definition of the North Pole to align the z-axis as shown in shown in Figure 1. Unlike the i-frame, the e-frame is not a fixed frame but has a rate of rotation Ω given by the rate of rotation of the e-frame about the Z-axis with respect to the i-frame. This is due to the horizontal axis being defined to fixed a point on the Earth. The e-frame uses the intersection of the Greenwich Meridian at the equator to define the x-axis while the y axis is defined to be 90° off the x-axis along the equator.

2.2.3 Navigation Frame

The Earth-fixed navigation frame or n-frame is a local reference frame that sets its origin at some predetermined point, usually with that point being located near the surface of the Earth. Since this frame's origin is stationary with a point on the earth, there is a turning rate of the n-frame with respect to the e-frame (referred to as the transportation rate identified by ω_{en} throughout this thesis.) This frame is useful for navigating over relatively short distances but provides a possibility to reduce the complexity of solving for a navigation solution.

The n-frame, can have several different orientations, while typically the North,

East and Down (NED) or the East, North, and Up (ENU) shown in Figure 1 are the two most commonly used orientation conventions. The NED orientation aligns the Down or z axis with that of gravity. With the x and y axes aligned with the North and East directions respectively. The ENU orientation is similar to the aforementioned NED Orientation, but x and y axes are reversed and correspond to the East and North Direction respectively, while the z axis aligned with the up direction to maintain the right-hand orthogonality to the x and y axes.

2.2.4 Body Frame

The body frame, or b-frame, is a reference frame that is affixed to the object that is being navigated with the frames, origin usually corresponding with that of the objects center of mass. The x, y, and z axes for this frame correspond with the affixed objects roll, pitch and yaw respectively. The raw values and measurements from any sensor, particularly accelerometers and gyroscopes, are taken from this frame and translated into another frame to solve an objects kinematic motion to get its position, velocity, and attitude over time.

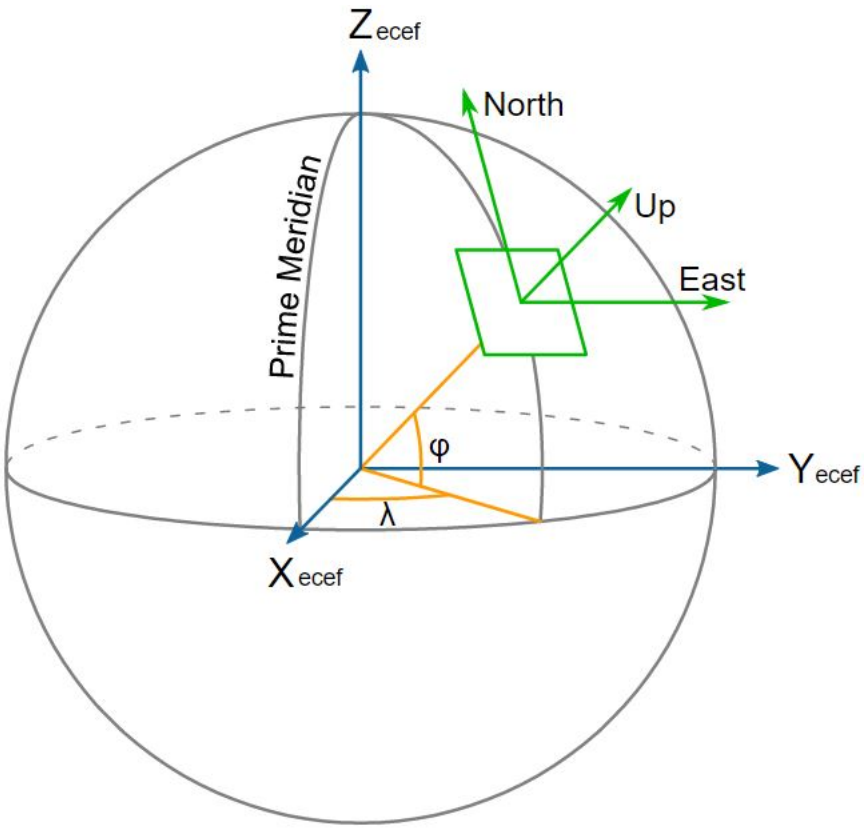

Figure 1: The ECEF and ENU Reference Frames.(Public domain usage from Wikipedia)

2.3 Coordinate Transformations

A coordinate transformation is utilized in order to resolve any measurements taken in one reference and convert those measurements to be used for computations in another reference. This transformation consists of a transformation between the coordinate frame origins and a rotation to align the axes. The rotation is often expressed as a 3x3 matrix referred to as a Direction Cosine Matrix (DCM). An example DCM is shown in Equation 2.1. This DCM indicates that the subscript ENU orientation of the n-frame is the frame that a system is being translated from, and the super script

NED orientation is the n-frame that is being translated to.

$$C_{ENU}^{NED} = \begin{bmatrix} 0 & 1 & 0 \\ 1 & 0 & 0 \\ 0 & 0 & -1 \end{bmatrix} \tag{2.1}$$

The simple example shown below in Equation 2.2 shows that if you have a velocity vector that is orientated in the ENU reference frame you can apply a DCM like the one shown by Equation 2.1 to get the velocity vector in the NED frame.

$$\begin{bmatrix} Velocity_E \\ Velocity_N \\ Velocity_U \end{bmatrix} \times C_{ENU}^{NED} = \begin{bmatrix} Velocity_N \\ Velocity_E \\ Velocity_D \end{bmatrix} \tag{2.2}$$

Additionally, the example shows in Equation 2.3 these types of transformation can be applied multiple times to translate between frames that do not have a direct translation or as required to format data in different frames for computational reasons.

$$\begin{bmatrix} Velocity_x \\ Velocity_y \\ Velocity_z \end{bmatrix} \times C_{body}^{ENU} \times C_{ENU}^{NED} = \begin{bmatrix} Velocity_N \\ Velocity_E \\ Velocity_D \end{bmatrix} \tag{2.3}$$

2.4 Inertial Navigation

This section reviews a brief mathematical description of inertial systems, their components, system mechanization, and the related strap-down errors. The component models, along with their system mechanization and related errors, is required for utilization in a Kalman filter solution. The sections that follow are written very similarly to [10, 11] and [12]. which is based on the text "*Strapdown Inertial Navigation Technology*" by Titterton and Weston.[9]. While the same information can be

found in these references, it is included here for completeness.

2.4.1 Inertial Measurement Unit (IMU)

To perform inertial navigation using an Inertial Navigation System (INS) a system processor and an Inertial Measurement Unit (IMU) is required. A Micro-electromechanical Systems (MEMS) based IMU which consists of a tri-axis accelerometer and a tri-axis gyroscope is utilized for this research. While some IMUs will also have a tri-axis magnetometer, the IMU used for the research does not. In the sub-sections that follow, the dynamics model for these IMUs used in the KF Filter are presented.

2.4.1.1 Accelerometers and Gyroscopes

The accelerometers found in an IMU measure specific forces in their respective axis. A specific force is any force exerted on the system except for gravity (gravity is not specific to the system, but instead exerted on all materials and therefore cannot be measured by the accelerometers.) The rate gyroscopes found in an IMU measure the angular rate of rotation about a specific axis in its body frame. Within an IMU, each of the accelerometers and gyroscopes is positioned such that the axis in which they are getting measurements is orthogonal to the other elements. Depending on the real-world accelerometers and gyroscopes' quality and sensitivity, measurements taken can have noticeable noise and biases resulting in measurement errors. These errors can be modeled and are concisely described in the research done by [10, 13].

2.4.2 Navigation Equations

For this thesis, the Navigation or n-frame described in 2.2.3 is utilized and, therefore, will be the chosen coordinate frame used for analysis in this section. A systems' given acceleration in the n-frame is expressed in Equation 2.4.

$$\dot{\boldsymbol{v}}_e^n = \boldsymbol{f}^n - (2\omega_{ie}^n + \omega_{en}^n) \times \boldsymbol{v}_e^n + \boldsymbol{g}_l^n \tag{2.4}$$

Where the first term f^n represents the measured accelerometer forces in the NED orientation and shown in component form in Equation 2.5

$$\boldsymbol{f}_n = \begin{bmatrix} f_N & f_E & f_D \end{bmatrix}^T \tag{2.5}$$

The second term $(2\omega_{en}^n + \omega_{en}^n) \times \boldsymbol{v}_e^n$ is known as the Coriolis acceleration, which models any apparent forces from the use of the rotating n-frame. Within this second term v_e^n is the systems velocity with respect to the Earth in the NED orientation as show in Equation 2.6

$$\boldsymbol{v}_e^n = \begin{bmatrix} v_N & v_E & v_D \end{bmatrix}^T \tag{2.6}$$

The Earths turn rate represented in the local frame is ω_{ie}^n. ω_{en}^n is the turn rate of the local frame with respect to the earth known as the transport rate. They are defined in in Equations 2.7 and 2.8 respectively where and L, ℓ are the systems Latitude and Longitude.

$$\omega_{ie}^n = \begin{bmatrix} \Omega \cos L & 0 & -\Omega \sin L \end{bmatrix}^T \tag{2.7}$$

$$\omega_{en}^n = \begin{bmatrix} \dot{\ell} \cos L & -\dot{L} & -\dot{\ell} \sin L \end{bmatrix} \tag{2.8}$$

The transport rate ω_{en}^n from Equation 2.8 can be rewritten in terms of the systems velocity in the n-frame shown in Equation 2.9 using the relations given in Equation 2.10

$$\omega_{en}^n = \begin{bmatrix} \frac{v_e}{R_0+h} & \frac{-v_n}{R_0+h} & \frac{-v_e \tan L}{R_0+h} \end{bmatrix}^T \tag{2.9}$$

$$\dot{L} = \frac{v_N}{R_0+h}, \quad \dot{\ell} = \frac{v_E \sec L}{R_0+h}, \quad \dot{h} = -v_D \tag{2.10}$$

where v_e and v_n are the North and East velocities, L & h are the systems latitude and height above the earth, and lastly R_0 is the radius of the earth.

The final term in Equation 2.4, g_l^n is the gravity vector in the local frame shown in Equation 2.11. This vector includes the effects of the mass attraction of the earth g and any centripetal accelerations due to the earth's rotations.

$$g_l^n = g - \omega_{ie} \times \omega_{ie} \times R = g - \Omega^2 \frac{(R_0 + h)}{2} \begin{pmatrix} \sin 2L \\ 0 \\ 1 + \cos 2L \end{pmatrix} \tag{2.11}$$

Given the equations above, the navigation equation can be broken down into its component form as shown in Equation 2.12. ξ and η are the respective angular deflections of the local gravity vector with respect to the reference frames vertical direction with $\dot{L}$, $\dot{\ell}$, and $\dot{h}$ are as described in Equation 2.10.

$$\begin{aligned} \dot{\boldsymbol{v}_n} &= f_N - 2\Omega v_E \sin L + \tfrac{v_N v_D - v_E^2 \tan L}{R_0+h} + \xi g \\ \dot{\boldsymbol{v}_E} &= f_E + 2\Omega(v_N \sin L + v_D \cos L) + \tfrac{v_E}{R_0+h}(v_D + v_N \tan L) - \eta g \\ \dot{\boldsymbol{v}_D} &= f_D - 2\Omega v_E \cos L - \tfrac{v_E^2 + v_N^2}{R_0+h} + g \end{aligned} \tag{2.12}$$

Given that any measurements provided from an IMU are in that IMUs body frame a rotation must be provided to utilize the Equations 2.4 - 2.12 presented above. This modification to Equation 2.4 provides Equation 2.13 in which the accelerations given by the IMU can be used.

$$\dot{\boldsymbol{v}_e^n} = \boldsymbol{C}_b^n \boldsymbol{f}^b - (2\omega_{ie}^n + \omega_{en}^n) \times \boldsymbol{v}_e^n + \boldsymbol{g}_l^n \tag{2.13}$$

Where the DCM $\boldsymbol{C}_b^n$ is used to relate the specific forces from the b-frame to the n-frame, and is kept up to date using Equation 2.14.

$$\dot{\boldsymbol{C}}_b^n = \boldsymbol{C}_b^n \boldsymbol{\Omega}_{nb}^b \tag{2.14}$$

Provided that $\boldsymbol{\Omega}_{nb}^b$ is the skew symmetric representation of body's rotation rate with respect to the navigation frame $\boldsymbol{\omega}_{nb}^b$ and is computed by Equation 2.15. With $\boldsymbol{\omega}_{ib}^b$ representing any measured rotations of the body itself.

$$\boldsymbol{\omega}_{nb}^b = \boldsymbol{\omega}_{ib}^b - \boldsymbol{C}_n^b[\boldsymbol{\omega}_{ie}^n + \boldsymbol{\omega}_{en}^n] \tag{2.15}$$

2.4.3 Navigation Error Equations

When designing or using a filtered solution, the navigation equations described in the previous section are not practical for implementation.[9, 10] This is because the system's errors limit an inertial navigation system.[9] The development of a general set of error equations have been derived for navigation within close proximity to the Earth using a local reference frame.[9]. This section is a consolidated representation of the general error equations derivation that is presented in [9].

2.4.3.1 Attitude Errors

In a strapdown system the actual orientation of a given system is represented by the DCM $\boldsymbol{C}_b^n$ representing orientation of the body frame into a navigation frame. An estimated attitude $\tilde{\boldsymbol{C}}_b^n$ is computed by Equation 2.16 where the $\boldsymbol{B}$ is a matrix that represents the misalignment relationship between a true reference axis and an estimated reference axis.

$$\tilde{\boldsymbol{C}}_b^n = \boldsymbol{B}\boldsymbol{C}_b^n \tag{2.16}$$

This misalignment relationship matrix, if small enough, can be approximated by the skew symmetric matrix Ψ as shown in Equation 2.17.

$$\boldsymbol{B} = [\boldsymbol{I} - \boldsymbol{\Psi}] \tag{2.17}$$

where $\boldsymbol{I}$ is a $3x3$ identity matrix, $\boldsymbol{\Psi}$ is shown in Equation 2.18, and α and β are the errors in attitudes with respect to pitch and roll and γ is the errors the heading or rotation about the vertical axis with respect to the NED reference frame.

$$\boldsymbol{\Psi} = \begin{bmatrix} 0 & -\delta\gamma & \delta\beta \\ \delta\gamma & 0 & -\delta\alpha \\ -\delta\beta & \delta\alpha & 0 \end{bmatrix} \tag{2.18}$$

Taking Equations 2.16 and 2.17 and combining them, the estimated direction cosine matrix can be rewritten as shown in Equation 2.19

$$\tilde{\boldsymbol{C}}_{\boldsymbol{b}}^{\boldsymbol{n}} = [\boldsymbol{I} - \boldsymbol{\Psi}]\, \boldsymbol{C}_{\boldsymbol{b}}^{\boldsymbol{n}} \tag{2.19}$$

Taking the rewritten estimated DCM, solving for $\boldsymbol{\Psi}$ and differentiating yields the $\dot{\boldsymbol{\Psi}}$ shown in Equation 2.20

$$\dot{\boldsymbol{\Psi}} = -\dot{\tilde{\boldsymbol{C}}}_{\boldsymbol{b}}^{\boldsymbol{n}} \boldsymbol{C}_{\boldsymbol{b}}^{\boldsymbol{n}T} - \tilde{\boldsymbol{C}}_{\boldsymbol{b}}^{\boldsymbol{n}} \dot{\boldsymbol{C}}_{\boldsymbol{b}}^{\boldsymbol{n}T} \tag{2.20}$$

The estimated DCM $\boldsymbol{C}_{\boldsymbol{b}}^{\boldsymbol{n}}$ propagates as a function of the absolute body rate and navigation frame rates represented by $\boldsymbol{\Omega}_{\boldsymbol{ib}}^{\boldsymbol{b}}$ and $\boldsymbol{\Omega}_{\boldsymbol{in}}^{\boldsymbol{n}}$ respectively and is expressed below in Equation 2.21.

$$\dot{\boldsymbol{C}}_{\boldsymbol{b}}^{\boldsymbol{n}} = \boldsymbol{C}_{\boldsymbol{b}}^{\boldsymbol{n}} \boldsymbol{\Omega}_{\boldsymbol{ib}}^{\boldsymbol{b}} - \boldsymbol{\Omega}_{\boldsymbol{in}}^{\boldsymbol{n}} \boldsymbol{C}_{\boldsymbol{b}}^{\boldsymbol{n}} \tag{2.21}$$

The estimated $\tilde{\boldsymbol{C}}_{\boldsymbol{b}}^{\boldsymbol{n}}$ propagation shown below in Equation 2.22 is similar to the

propagation of $\boldsymbol{C_b^n}$ except that the estimate DCM is propagated with respect to the estimated body $\tilde{\boldsymbol{\Omega}}_{\boldsymbol{ib}}^{\boldsymbol{b}}$ and navigation frame rates $\tilde{\boldsymbol{\Omega}}_{\boldsymbol{in}}^{\boldsymbol{n}}$

$$\dot{\tilde{\boldsymbol{C}}}_{\boldsymbol{b}}^{\boldsymbol{n}} = \tilde{\boldsymbol{C}}_{\boldsymbol{b}}^{\boldsymbol{n}} \tilde{\boldsymbol{\Omega}}_{\boldsymbol{ib}}^{\boldsymbol{b}} - \tilde{\boldsymbol{\Omega}}_{\boldsymbol{in}}^{\boldsymbol{n}} \tilde{\boldsymbol{C}}_{\boldsymbol{b}}^{\boldsymbol{n}} \tag{2.22}$$

Taking the definitions of $\dot{\boldsymbol{C}}_{\boldsymbol{b}}^{\boldsymbol{n}}$ and $\dot{\tilde{\boldsymbol{C}}}_{\boldsymbol{b}}^{\boldsymbol{n}}$ from Equations 2.21 and 2.22 respectively and substituting them into Equation 2.20 yields Equation 2.23 when simplified.

$$\dot{\boldsymbol{\Psi}} = -\tilde{\boldsymbol{C}}_{\boldsymbol{b}}^{\boldsymbol{n}} \left[\tilde{\boldsymbol{\Omega}}_{\boldsymbol{ib}}^{\boldsymbol{b}} - \boldsymbol{\Omega}_{\boldsymbol{ib}}^{\boldsymbol{b}} \right] \boldsymbol{C}_{\boldsymbol{b}}^{\boldsymbol{n}T} + \tilde{\boldsymbol{\Omega}}_{\boldsymbol{in}}^{\boldsymbol{n}} \tilde{\boldsymbol{C}}_{\boldsymbol{b}}^{\boldsymbol{n}} \boldsymbol{C}_{\boldsymbol{b}}^{\boldsymbol{n}T} - \tilde{\boldsymbol{C}}_{\boldsymbol{b}}^{\boldsymbol{n}} \boldsymbol{C}_{\boldsymbol{b}}^{\boldsymbol{n}T} \boldsymbol{\Omega}_{\boldsymbol{in}}^{\boldsymbol{n}} \tag{2.23}$$

Replacing $\dot{\tilde{\boldsymbol{C}}}_{\boldsymbol{b}}^{\boldsymbol{n}}$ in Equation 2.23 results in Equation 2.24

$$\dot{\boldsymbol{\Psi}} = -\left[\boldsymbol{I} - \boldsymbol{\Psi}\right] \boldsymbol{C}_{\boldsymbol{b}}^{\boldsymbol{n}} \left[\tilde{\boldsymbol{\Omega}}_{\boldsymbol{ib}}^{\boldsymbol{b}} - \boldsymbol{\Omega}_{\boldsymbol{ib}}^{\boldsymbol{b}} \right] \boldsymbol{C}_{\boldsymbol{b}}^{\boldsymbol{n}T} + \tilde{\boldsymbol{\Omega}}_{\boldsymbol{in}}^{\boldsymbol{n}} \left[\boldsymbol{I} - \boldsymbol{\Psi}\right] \boldsymbol{C}_{\boldsymbol{b}}^{\boldsymbol{n}} \boldsymbol{C}_{\boldsymbol{b}}^{\boldsymbol{n}T} - \left[\boldsymbol{I} - \boldsymbol{\Psi}\right] \boldsymbol{C}_{\boldsymbol{b}}^{\boldsymbol{n}} \boldsymbol{C}_{\boldsymbol{b}}^{\boldsymbol{n}T} \boldsymbol{\Omega}_{\boldsymbol{in}}^{\boldsymbol{n}} \tag{2.24}$$

By substituting the differences between the estimated values and the actual values with δ and ignoring the error product terms the Equation 2.24 can be re written as shown in Equation 2.25

$$\dot{\boldsymbol{\Psi}} \approx \boldsymbol{\Psi} \boldsymbol{\Omega}_{\boldsymbol{in}}^{\boldsymbol{n}} - \boldsymbol{\Omega}_{\boldsymbol{in}}^{\boldsymbol{n}} \boldsymbol{\Psi} + \boldsymbol{\delta} \boldsymbol{\Omega}_{\boldsymbol{in}}^{\boldsymbol{n}} - \boldsymbol{C}_{\boldsymbol{b}}^{\boldsymbol{n}} \boldsymbol{\delta} \boldsymbol{\Omega}_{\boldsymbol{ib}}^{\boldsymbol{b}} \boldsymbol{C}_{\boldsymbol{b}}^{\boldsymbol{nT}} \tag{2.25}$$

or it can be expressed in its vector form as shown in Equation 2.26 such that Ψ is the misalignment vector $\begin{bmatrix} \delta\alpha & \delta\beta & \delta\gamma \end{bmatrix}$ and $\omega\times = \Omega$

$$\dot{\Psi} \approx -\omega_{in}^{n} \times \Psi + \delta\omega_{in}^{n} - C_{b}^{n} \delta\omega_{ib}^{b} \tag{2.26}$$

2.4.3.2 Velocity and Position Errors

The velocity equation shown below represented in Equation 2.27 is the same equation for acceleration shown in Equation 2.13 previously.

$$\dot{\boldsymbol{v}_e^n} = \boldsymbol{C}_n^b \boldsymbol{f}^b - (2\omega_{ie}^n + \omega_{en}^n) \times \boldsymbol{v} + \boldsymbol{g}_l \tag{2.27}$$

A computed estimation of the velocities $\dot{\tilde{\boldsymbol{v}}_e^n}$ can be derived with the assumption made that the estimation propagates similarity to Equation 2.27 using estimated values.

$$\dot{\tilde{\boldsymbol{v}}_e^n} = \tilde{\boldsymbol{C}}_n^b \tilde{\boldsymbol{f}}^b - (2\tilde{\omega}_{ie}^n + \tilde{\omega}_{en}^n) \times \tilde{\boldsymbol{v}} + \tilde{\boldsymbol{g}}_l \tag{2.28}$$

The results of taking the difference between Equation 2.28 and Equation 2.27 provides a delta as shown in Equation 2.29

$$\boldsymbol{\delta \dot{v}} = \tilde{\boldsymbol{C}}_{\boldsymbol{n}}^{\boldsymbol{b}} \tilde{\boldsymbol{f}}^{\boldsymbol{b}} - \boldsymbol{C}_{\boldsymbol{b}}^{\boldsymbol{n}} \boldsymbol{f}^{\boldsymbol{b}} - (\boldsymbol{2}\tilde{\boldsymbol{\omega}}_{\boldsymbol{ie}}^{\boldsymbol{n}} + \tilde{\boldsymbol{\omega}}_{\boldsymbol{en}}^{\boldsymbol{n}}) \times \tilde{\boldsymbol{v}} + (\boldsymbol{2\omega}_{\boldsymbol{ie}}^{\boldsymbol{n}} + \boldsymbol{\omega}_{\boldsymbol{en}}^{\boldsymbol{n}}) \times \boldsymbol{v} + \tilde{\boldsymbol{g}}_{\boldsymbol{l}} - \boldsymbol{g}_{\boldsymbol{l}} \tag{2.29}$$

By replacing $\tilde{\boldsymbol{C}}_{\boldsymbol{n}}^{\boldsymbol{b}}$ with $[\boldsymbol{I} - \boldsymbol{\Psi}]\, \boldsymbol{C}_{\boldsymbol{b}}^{\boldsymbol{n}}$ and substituting the differences between the estimated values and their true values with δs while ignoring the products of the error terms, Equation 2.30 is formed.

$$\boldsymbol{\delta \dot{v}} = -\boldsymbol{\Psi C}_{\boldsymbol{b}}^{\boldsymbol{n}} \boldsymbol{f}^{\boldsymbol{b}} + \boldsymbol{C}_{\boldsymbol{b}}^{\boldsymbol{n}} \boldsymbol{\delta f}^{\boldsymbol{b}} - (\boldsymbol{2\omega}_{\boldsymbol{ie}}^{\boldsymbol{n}} + \boldsymbol{\omega}_{\boldsymbol{en}}^{\boldsymbol{n}}) \times \boldsymbol{\delta v} - (\boldsymbol{2\delta\omega}_{\boldsymbol{ie}}^{\boldsymbol{n}} + \boldsymbol{\delta\omega}_{\boldsymbol{en}}^{\boldsymbol{n}}) \times \boldsymbol{v} - \boldsymbol{\delta g} \tag{2.30}$$

If there is an assumption that there is some knowledge of the gravity vector, ignoring the errors in the Coriolis terms, and substituting $\boldsymbol{C}_{\boldsymbol{b}}^{\boldsymbol{n}} \boldsymbol{f}^{\boldsymbol{b}}$ with f^n the Equation 2.30 can be further reduced as shown by Equation 2.31

$$\boldsymbol{\delta \dot{v}} = [\boldsymbol{f}^{\boldsymbol{n}} \times]\, \Psi + \boldsymbol{C}_{\boldsymbol{b}}^{\boldsymbol{n}} \boldsymbol{\delta f}^{\boldsymbol{b}} \tag{2.31}$$

The position errors $\boldsymbol{\delta P}$ are shown in the equation below as a function of the velocity errors $\boldsymbol{\delta v}$.

$$\boldsymbol{\delta \dot{P}} = \boldsymbol{\delta v} \tag{2.32}$$

The Equations 2.26, 2.30, and 2.32 are combined to form the basis of the Pinson Error model shown in Equation 2.33, where Equation 2.33 shows the propagation matrix given the state vector $\delta x = [\boldsymbol{\delta\Psi}, \boldsymbol{\delta v}, \boldsymbol{\delta P}]^T$.

$$\begin{bmatrix}
0 & -(\Omega\sin L+\frac{v_e}{R}\tan L) & \frac{v_n}{R} & 0 & \frac{1}{R} & 0 & -\Omega\sin L & 0 & -\frac{v_e}{R^2} \\
(\Omega\sin L+\frac{v_e}{R}\tan L) & 0 & -(\Omega\cos L+\frac{v_e}{R}) & -\frac{1}{R} & 0 & 0 & 0 & 0 & \frac{v_n}{R^2} \\
-\frac{v_n}{R} & (\Omega\cos L+\frac{v_e}{R}) & 0 & 0 & -\frac{\tan L}{R} & 0 & -\Omega\cos L-\frac{v_e}{R\cos^2 L} & 0 & \frac{v_e\tan L}{R^2} \\
0 & -f_d & f_e & \frac{v_d}{R} & -2(\Omega\sin L+\frac{v_e}{R}\tan L) & \frac{v_n}{R} & -v_e(2\Omega\cos L-\frac{v_e}{R\cos^2 L}) & 0 & \frac{1}{R^2}(v_e^2\tan L-v_nv_d) \\
f_d & 0 & -f_n & 2\Omega\sin L+\frac{v_e}{R}\tan L & \frac{1}{R}(v_n\tan L+v_d) & 2(\Omega\cos L+\frac{v_e}{R}) & 2\Omega(v_n\cos L-v_d\sin L)+\frac{v_nv_e}{R\cos^2 L} & 0 & -\frac{v_e}{R^2}(v_n\tan L+v_d) \\
-f_e & f_n & 0 & -\frac{2v_n}{R} & -2(\Omega\cos L+\frac{v_e}{R}) & 0 & 2\Omega v_e\sin L & 0 & \frac{1}{R^2}(v_n^2+v_e^2) \\
0 & 0 & 0 & \frac{1}{R} & 0 & 0 & 0 & 0 & -\frac{v_n}{R^2} \\
0 & 0 & 0 & 0 & \frac{1}{R\cos L} & 0 & \frac{v_e\tan L}{R\cos L} & 0 & -\frac{v_e}{R^2\cos L} \\
0 & 0 & 0 & 0 & 0 & -1 & 0 & 0 & 0
\end{bmatrix} \tag{2.33}$$

2.5 Kalman Filtering

The following section closely adheres to the information presented in [14] and [10] which are based on the information provided in [15], [16], and [17] where further detail and proofs can be found.

A KF is an optimal linear estimator that utilizes a recursive approach that combines the known system dynamics and any measurement data available to estimate the desired variables.[15] The technical foundation for all KF variants is the linear KF, discussed in 2.5.1. This research focuses on the utilization of the EKF which will be discussed in Section 2.5.2.

2.5.1 Linear Kalman Filter

Linear KF has the hard requirement of linear dynamics and measurements for the entire system. The basic KF equations for dynamics and the measurements are shown below in Equations 2.34 - 2.37

KFs have the same structure and consist of the propagate and update steps. The Propagation step takes the known system dynamics and any prior knowledge of the systems states and provides a prediction of those states at some given future time-based. The amount of uncertainty or the system's covariance of the prediction will continually increase unless a measurement is provided to the system. That leads to the second step of the KF process, the Update. This step takes any given measurement data at a given time, and its corresponding uncertainty and optimally incorporates that data to improve the estimated states after a propagation.

The dynamics in continuous time are described by Equation 2.34 where $\boldsymbol{x}(t)$ is the is the state process with N elements, $\mathbf{F}(t)$ is the $\mathbf{N} \times \mathbf{N}$ matrix modeling the system's state dynamics, $\mathbf{u}(t)$ is the input vector with length R, the $\mathbf{N} \times \mathbf{R}$ input matrix $\mathbf{B}(t)$, $\mathbf{w}(t)$ is the noise vector with length S that represents the zero mean

White Gaussian Noise (WGN) and the accompanying $\mathbf{N} \times \mathbf{S}$ noise matrix $\mathbf{G}(t)$.[15]

$$\dot{\mathbf{x}}(t) = \mathbf{F}(t)\mathbf{x}(t) + \mathbf{B}(t)\mathbf{u}(t) + \mathbf{G}(t)\mathbf{w}(t) \tag{2.34}$$

Most real-world systems, like IMUs, are not continuous but are taken at some sampling rate a discrete time dynamics model formed as shown in 2.35. In this form $\mathbf{B_d}$ and $\mathbf{w_d}$ are the discrete $\mathbf{N} \times \mathbf{S}$ input and length $\mathbf{S}$ discrete noise matrices respectively, while $\mathbf{\Phi}(t_i)$ is a discrete implementation of the continuous state dynamics $\mathbf{F}(t)$ which is defined by Equation 2.36.

$$\mathbf{x}(t_{i-1}) = \mathbf{\Phi}(t_i)\mathbf{x}(t_i) + \mathbf{B_d}(t_i)\mathbf{u}(t_i) + \mathbf{w_d}(t_i) \tag{2.35}$$

$$\mathbf{\Phi} = e^{\boldsymbol{F}\triangle t} \tag{2.36}$$

Lastly, unlike the system dynamics the measurement function is already inherently a discrete function with the measurement vector $\mathbf{Z}$ that has a length equal to the number of measurements provided ($\mathbf{M}$) and is only valid for a given time t_i. The $\mathbf{H}(t_i)$ is the $\mathbf{M} \times \mathbf{N}$ measurement matrix that maps the state $\mathbf{x}(t)$ at time $\mathbf{t_i}$ to the measurement $\mathbf{z}(t_i)$. $\mathbf{v}(t_i)$ is a $\mathbf{M}$ length vector for the zero mean WGN associated with each measurement.

$$\mathbf{z}(t_i) = \mathbf{H}(t_i)\mathbf{x}(t_i) + \mathbf{v}(t_i) \tag{2.37}$$

2.5.1.1 Propagate

Equations 2.38 - 2.40 are the equations used to propagate a set of states forward in time. For notation purposes in the KF section the superscript "-" and "+" denotes the estimate before and after an update is applied

$$\boldsymbol{x}_i^- = \boldsymbol{\Phi}_{i-1}\hat{\boldsymbol{x}}_{i-1}^+ + \int_{t_{i-1}}^{t_i} \boldsymbol{\Phi}(t_{i-1},\tau)\boldsymbol{B}(\tau)\boldsymbol{u}(\tau)d\tau \tag{2.38}$$

$$P_t^- = \boldsymbol{\Phi}_{i-1}P_{i-1}^+\boldsymbol{\Phi}_{i-1}^T + Q_d \tag{2.39}$$

$$Q_d = \int_{t_i-1}^{t_i} \boldsymbol{\Phi}(t_i-\tau)\boldsymbol{GQ}(\tau)\boldsymbol{G}^T\boldsymbol{\Phi}(t_i-\tau)^T d\tau \tag{2.40}$$

2.5.1.2 Update

Equations 2.41 - 2.44 are the update equations. Equation 2.41 is the Kalman filter gain and is how the filter estimates how much weight should be on the current set of measurements.

$$\boldsymbol{K}_i = \boldsymbol{P}_i^-\mathbf{H}^T[\mathbf{H}\mathbf{P}_i^-\mathbf{H}^T + \mathbf{R}_i]^{-1} \tag{2.41}$$

In the equations below, the KF gain in employed to update the system state estimate and corresponding covariance. $\mathbf{r}$ in Equation 2.43 is the residuals which represents the difference between the predicted values that were estimated ($\mathbf{H}\hat{x}$) and the actual values from any measurements provided z_i.

$$\hat{\boldsymbol{x}}_i^+ = \hat{\boldsymbol{x}}_i^- + \boldsymbol{K}_i\boldsymbol{r}_i \tag{2.42}$$

$$\boldsymbol{r}_i = \boldsymbol{z}_i - \boldsymbol{H}_i\hat{\boldsymbol{x}}_i^- \tag{2.43}$$

$$\boldsymbol{P}_i^+ = \boldsymbol{P}_i^- - \boldsymbol{K}_i\boldsymbol{H}\boldsymbol{P}_i^- \tag{2.44}$$

After all available measurements have been applied, the update process is completed, and the new system estimate is formed after which the process is then repeated.

2.5.2 Extended Kalman Filter (EKF)

For the most part, natural systems in the world cannot be modeled using only a set of linear dynamics. As mentioned in Section 2.5 this research focuses on the use of the EKF which was developed to handle systems that have nonlinear dynamics. The EKF has some of the same underlying principles that are found in the KF, such as the assumption of additive zero-mean WGN. Other parts, such as the dynamics of the now nonlinear system, and measurements are shown in Equations 2.45 and 2.46 respectively.

$$\dot{\boldsymbol{x}}(t) = \boldsymbol{f}[\boldsymbol{x}(t), u(t), t] + \boldsymbol{G}(t)\boldsymbol{w}(t) \tag{2.45}$$

$$\boldsymbol{z}(t) = \boldsymbol{h}[\boldsymbol{x}(t_i), t_i] + \boldsymbol{v}(t_i) \tag{2.46}$$

To implement the EKF, these system states are linearized about a nominal estimate to account for the new dynamics which provides a nominal system dynamics shown in Equation 2.47 and a measurement dynamics equation shown in Equation 2.48.

$$\dot{\boldsymbol{x}_n}(t) = \boldsymbol{f}[\boldsymbol{x}_n(t), \boldsymbol{u}(t)] + \left.\frac{\delta \boldsymbol{f}(\boldsymbol{x}, \boldsymbol{u}, t)}{\delta \boldsymbol{x}(t)}\right|_{x=x_n(t)} \delta\boldsymbol{x}(t) + \boldsymbol{G}(t)\boldsymbol{w}(t) \tag{2.47}$$

$$\boldsymbol{z}_n(t) = \boldsymbol{h}[\boldsymbol{x}_n(t_i), t_i] + \left.\frac{\delta \boldsymbol{h}(\boldsymbol{x}, \boldsymbol{u}, t_i)}{\delta \boldsymbol{x}(t_i)}\right|_{x=x_n(t_i)} \delta\boldsymbol{x}(t_i) + \boldsymbol{v}(t_i) \tag{2.48}$$

Because this newly computed state $\dot{\boldsymbol{x}_n}$ is based off of a nominal solution it does not identically match the values of the true state. This results in the perturbation in

Equation 2.49, where F is the Jacobian of f and is computed according to Equation 2.50

$$\dot{\boldsymbol{\delta x}}(t) = \boldsymbol{F}[t; \boldsymbol{x_n}(t)]\boldsymbol{\delta x}(t) + \boldsymbol{G}(t)\boldsymbol{w}(t) \tag{2.49}$$

$$\boldsymbol{F}[t; \boldsymbol{x_n}(t)] = \frac{\delta \boldsymbol{f}[\boldsymbol{x}, \boldsymbol{u}(t), t]}{\delta \boldsymbol{x}}|_{\boldsymbol{x}=\boldsymbol{x_n}(t)} \tag{2.50}$$

Similar to the the nominal system dynamics the nominal measurement dynamics also has a perturbation model shown in Equation 2.51. The Jacobian from Equation 2.50 is applied similarly to h to compute H.

$$\boldsymbol{\delta z}(t_i) = \boldsymbol{H}[t; \boldsymbol{x_n}(t)]\boldsymbol{\delta x}(t_i) + \boldsymbol{v}(t_i) \tag{2.51}$$

The perturbation models enable the equations for the KF to be utilized with non-linear system models.[10] In doing so, the output of the system is the estimate of the total states defined as Equation 2.52. Where $\hat{\boldsymbol{x}}(t)$ denotes the best estimate of the total states and $\hat{\delta \boldsymbol{x}}(t)$ is the optimal estimate.

$$\hat{\boldsymbol{x}}(t) \triangleq \boldsymbol{x_n}(t) + \hat{\delta \boldsymbol{x}}(t) \tag{2.52}$$

2.5.2.1 Propagate

The EKF propagates forward in time the same as the KF except that the system is re-linearized after every update. This re-linearization minimizes the error in the estimated nominal trajectory.

2.5.2.2 Update

The update process like the propagate process is completed similar to that of the KF found in Section 2.5.1.2 with some modification to the measurement equations. For each of the measurements the Jacobian is taken, as shown in Equation 2.51 which forms the measurement equation shown in 2.53.

$$x_i = \hat{x}_i^- + K(z_i - h([\hat{x}_i^-]) \tag{2.53}$$

Once the new measurement equations are calculated the Kalman gain $\boldsymbol{K}$ and $\boldsymbol{P}$ are computed utilizing the KF Equations 2.41 and 2.44 respectively.

2.6 Zero Velocity Update

An essential concept in implementing PDR is the concept of a Zero Velocity Update (ZUPT) which is a solution to help minimize the sensor drift.[18]. The basic concept behind the ZUPT is that when walking/running, when the foot of a person is on the ground, that foot is not moving, i.e., has zero velocity.

According to Abdulrahim et al. [19] ZUPTs can be implemented in one of two ways: first, a conventional dead reckoning is implemented, but the velocity data is simply zeroed out when a stance phase is detected. The second uses an estimation algorithm to estimate the sensors' errors using a zero velocity "measurement" as an update to the overall system state (including velocity.) A step detection algorithm is required to detect the stance phase of a gait in both cases, as shown in Figure 2. We perform updates using the second approach (a zero velocity "measurement" is created) in this thesis using an error model that is discussed in Section 3.3.1. The step detection algorithm's specifics are discussed further in sections 3.6.

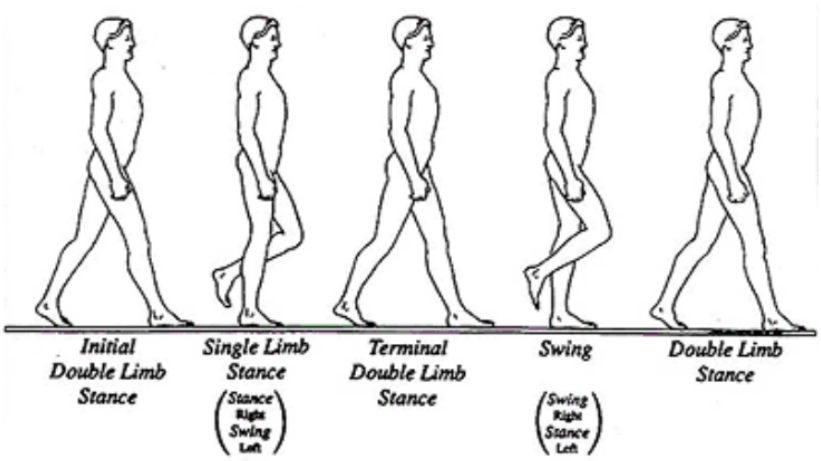

Figure 2: The complete gate cycle from [1]

2.7 Related Research

This section details the relevant previous research done while noting the areas in which this thesis uses to builds a testbed. As alluded to in 1.3 there have been several different methods that have been researched to attempt to solve this difficult problem. This thesis takes the research previously accomplished and groups them into Single and Multi IMU PDR categories.

2.7.1 Single IMU PDR

The research done by [8] and [20] shows that PDR can be accomplished using a single foot mounted IMU. From [8], the use of IMUs alone for dead reckoning is not enough to provide a reliable position tracking because the slightest gyro drift rate creates a positional error that has a cubical growth over time. To reduce the drift a ZUPT is used as described in the previous section. This combination of ZUPT single foot mounted IMU forms what this thesis might refer to as the "baseline" or "basic" form of PDR.

Other research, such as that presented in [20] and [21], has tried to continue

the utilization of single IMU PDR with extra sensors or by improving the step-detection and adding in a stride length estimation to limit the IMU drift. While this approach limits the amount of equipment a user has to wear, these approaches have the disadvantage of needing to be "calibrated" to the user.

Rather than requiring an IMU to be attached to a person's foot, many papers have attempted to use the IMU that most people carry around with them: their smartphone.[22] This "Single IMU" approach has its own set of advantages and disadvantages. The advantages start with the potential number of other co-located sensors used to aid the IMU such as WiFi Antennas, barometers, and temperature sensors. [22] One of the major disadvantages is that the smartphones can be held in various ways, limiting the viability of utilizing some of the foot-mounted IMU mechanization-based methods. To address the variety of orientations, some fairly computationally intensive methods, including machine learning, have been tried to achieve accurate PDR. [23, 24]

2.7.2 Multi IMU PDR

One possible method for improving the accuracy of a single IMU PDR system is to add more IMUs and see if the accuracy of the PDR solutions can be improved. In research such as [6] and [5], foot mounted IMUs (one on each foot) was the basis of their approach for conducting PDR. Recall from Section 1.3, Brand and Phillips present in [5] a PDR system using a system that utilized IMUs on each of the user's feet while using a "foot-to-foot" range measurements. Also, recall that this range measurement was accomplished by using a large frequency generator at the waist that sent signals down one leg to a transmitting antenna on one foot, which then sent that signal to a receiver on the other foot (which sent the signals back to the waist pack.)

In [6], Laverne et al. use several test cases to show that a more accurate PDR system is possible by using an independent pair of high-quality IMUs with a ranging constraint between them. Although this research proved this form of dual IMU PDR is feasible, it has the same weaknesses as [5] utilizing high quality and large components that would be too cumbersome and costly for a user to wear.

Other researchers have gone beyond and used several IMUs to model the entire lower portion of a human body for PDR. Research done by [25], [26], and [27] have taken this approach and placed IMUs on not only the feet but the shins, thighs, and waist, which improves the overall human motion modeling. For example, Lee et al. in [27] uses a system of seven IMUs which were able to get a relative yaw calculation by using the data from a waist-mounted IMU and accurately modeled the lower human motion with the others. These multi IMU have the disadvantage of an increased complexity because it requires an accurate kinematic system model and some form of data fusion algorithm to utilize that data in a PDR system.

In this thesis, we seek to utilize the foot-based PDR solution in [6]. We believe that the accuracy demonstrated in [6] is significantly better than single IMU systems, but is still less complex than (and thereby more feasible than) multi-IMU systems. Our research implements a testbed based on this type of foot-mounted solution to develop a wearable PDR solution. This testbed will allow for various sensors and techniques to be evaluated, such as replacing the previously mentioned higher-quality IMUs with a smaller size, weight, power, and cost IMUs or replacing the large RF-based foot-to-foot range measurements with smaller relative pose magnetic sensors.

III. Methodology

3.1 Overview

This purpose of this chapter is to provide a brief background of the underlying theories, conventions and techniques used in this research. Specifically, we will be overviewing the following items:

- Evaluation method for the Pedestrian Dead Reckoning (PDR) system.
- A background into the Scorpion Development Toolkit (STK).
- The architecture of the single Inertial Measurement Unit (IMU) PDR system
- The architecture of the two dual IMU PDR systems
- The step detection algorithm utilized for the Zero Velocity Update (ZUPT)
- The equipment used to collect the data.

3.2 Testing Framework

As stated in Section 1.4 that in order to evaluate and assess if the PDR testbed three PDR solutions are iteratively designed, and implemented utilizing the STK. Starting with the single IMU PDR solution discussed in 2.7.1 which utilizes, a single commercial grade IMU and the ZUPT algorithm. This single IMU is also used to ensure the step detection algorithm accurately identifies the steps taken for the accurate application of ZUPT. The step detection algorithm used for ZUPT is outlined in Section 3.6 with the model for the commercial grade IMU shown in Section 3.7.1

The iterative process starts with the single IMU PDR system. Once the single IMU PDR system is implemented successfully, the Dual IMU PDR systems is implemented

utilizing the same ZUPT algorithm as the single IMU PDR system. Lastly, the third system builds upon the Dual IMU PDR systems with the addition of a magnetic sensor that provided a foot-to-foot ranging measurement.

The assessment of these designs will be conducted through the post-processing of real-world data utilizing the STK, outlined in Section 3.3. The data-sets that will be evaluated are collected by (a) walking around a standard track or (b) around residential neighborhoods. Both data-sets will be collected using a custom-designed wearable system described in Section 3.7.3. The truth data for all the collected data-sets will be provided by a Global Positioning System (GPS) system carried around with the user. This GPS data will also provide updates during an initialization period for both the single and dual IMU PDR system to aid in the system's initial alignment. Additionally, for both the single and dual IMU systems, the same IMU models and step detection for ZUPT is used to ensure a fair comparison between the systems.

3.3 Scorpion Toolkit

In order to implement a Kalman Filter (KF) framework capable of handling multiple IMUs and measurements, we used the STK. The STK is a redesigned version of the Air Force Institute of Technology (AFIT) Scorpion Software Suite, which is a modular Bayesian estimation software toolkit. This Toolkit is designed for either real-time or post-processing sensor data and can be implemented with multiple languages [28]. This thesis will be using the Python interface to the STK.

This thesis utilizes both the standard "Whole-state" model and error state model when applying updates to the system. The STK easily allows for error models and standard "Whole-state" models to be utilized interchangeably. With this flexibility available, the PDR system can model the dynamics and propagate using the error model while having the versatility to apply measurements to the standard model or

error model. This modularity also enables the analysis of the PDR system to be done using either the standard model or the error model.

3.3.1 Pinson Error Model

The Extended Kalman Filter (EKF) implemented in STK for this research uses a 15 state error model referred to as the Pinson 15 Error Model. This section comes form [29], [11] and, [9], but several paragraphs in the section are almost direct quotes from [29]. The traditional Pinson model is the 9 state model that was previously discussed in Section 2.4.3. The 15 state model $\delta\boldsymbol{x}$ is outlined in Equation 3.1. This expands upon the traditional 9 states for the errors in the North, East and Down (NED) frame for position, velocity, and attitude of a system given as $\delta\boldsymbol{p}$, $\delta\boldsymbol{v}$, and $\delta\boldsymbol{\omega}$ respectively. This 9 state model is modified to also include the gyroscope and accelerometer bias errors $\delta\boldsymbol{b}_a$ and $\delta\boldsymbol{b}_\omega$ respectively. Noting that each of the elements of this matrix is a 3×1 matrix.

$$\boldsymbol{x} = \begin{bmatrix} \delta\boldsymbol{p}_{NED} \\ \delta\boldsymbol{v}_{NED} \\ \delta\boldsymbol{\omega}_{rpy} \\ \delta\boldsymbol{b}_a \\ \delta\boldsymbol{b}_\omega \end{bmatrix}_{15\times 1} \tag{3.1}$$

By taking equations 2.26, 2.30, and 2.32 and including the bias terms for the accelerometer $\delta\boldsymbol{b}_a$ and gyroscope $\delta\boldsymbol{b}_g$ modeled as random walk processes. The new 15 state dynamics model shown in Equation 3.2 below is formed by combining the 9 state dynamics model with the additional Biases.

$$\boldsymbol{F}_{P15ins} = \begin{bmatrix} \boldsymbol{F_{Pinson}}_{9\times9} & \mathbf{0}_{3\times3} & \mathbf{0}_{3\times3} \\ \mathbf{0}_{3\times3} & \boldsymbol{b_a}_{3\times3} & \mathbf{0}_{3\times3} \\ \mathbf{0}_{3\times3} & \mathbf{0}_{3\times3} & \boldsymbol{b_g}_{3\times3} \end{bmatrix}_{15\times15} \tag{3.2}$$

w defined by Equation 3.3 is the driving noise vector which is formed from the associated noise terms of the accelerometer and gyroscope measurement and bias. [12]

$$w = \begin{bmatrix} \mathbf{0}_{9\times1} \\ \boldsymbol{w_a}_{3\times1} \\ \boldsymbol{w_g}_{3\times1} \end{bmatrix}_{15\times1} \tag{3.3}$$

Given the noise vector from Equation 3.3 the noise matrix Q as show in Equation 3.4. Each of the elements of this matrix is a 3×3 matrix that corresponds to each of the NED elements of the **F** matrix.

$$\boldsymbol{Q} = \begin{bmatrix} \mathbf{0}_{3\times3} & \mathbf{0}_{3\times3} & \mathbf{0}_{3\times3} & \mathbf{0}_{3\times3} & \mathbf{0}_{3\times3} \\ \mathbf{0}_{3\times3} & \sigma^2_{a_{rw}}\boldsymbol{I}_{3\times3} & \mathbf{0}_{3\times3} & \mathbf{0}_{3\times3} & \mathbf{0}_{3\times3} \\ \mathbf{0}_{3\times3} & \mathbf{0}_{3\times3} & \sigma^2_{g_{rw}}\boldsymbol{I}_{3\times3} & \mathbf{0}_{3\times3} & \mathbf{0}_{3\times3} \\ \mathbf{0}_{3\times3} & \mathbf{0}_{3\times3} & \mathbf{0}_{3\times3} & \frac{2\sigma^2_{a_b}}{\tau_{a_b}}\boldsymbol{I}_{3\times3} & \mathbf{0}_{3\times3} \\ \mathbf{0}_{3\times3} & \mathbf{0}_{3\times3} & \mathbf{0}_{3\times3} & \mathbf{0}_{3\times3} & \frac{2\sigma^2_{g_b}}{\tau_{g_b}}\boldsymbol{I}_{3\times3} \end{bmatrix}_{15\times15} \tag{3.4}$$

This Noise matrix is then built and utilized in Scorpion using the specifications for the IMUs accelerometer and Gyroscope outlined in section 3.7.1.

3.4 Single IMU PDR

A block diagram of the how the system is designed is pictured below in Figure 3 following by an overview of how the system implemented.

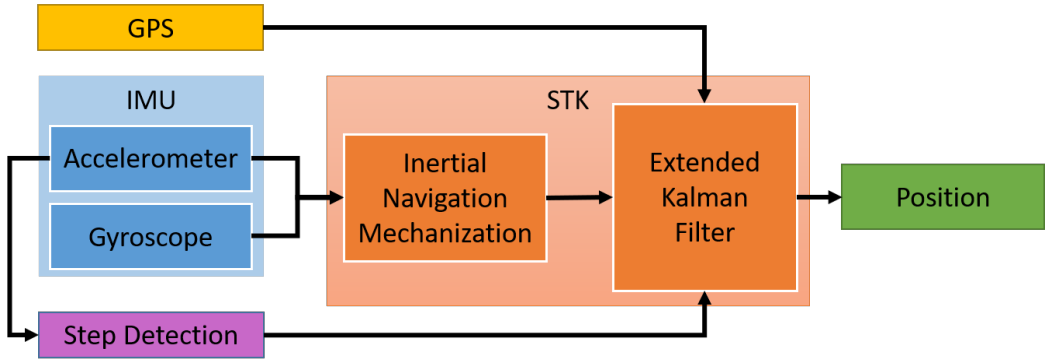

Figure 3: Block Diagram of the single IMU systems

For the single IMU PDR system accelerometer and gyroscope data from the IMU on the right foot is used and fed into the STK software where internal functions are used for mechanization, as well as the propagation and updating of the states in the EKF. The single IMU PDR system's filter design uses the Pinson 15 states and dynamics matrix outlined in section 3.3.1 using the IMU specifications displayed in Table 1. The only update that is applied to the filtered system for the single IMU PDR solution is the ZUPT to reduce the drift of the IMU. The ZUPT measurement z shown in Equation 3.5 is the velocity in the NED orientation at a given time step where the step detection algorithm has identified a step, indicating there is no movement of the foot.

$$\boldsymbol{z} = \begin{bmatrix} \mathbf{0} \\ \mathbf{0} \\ \mathbf{0} \end{bmatrix} \tag{3.5}$$

This ZUPT is applied to the velocity terms in the Pinson states through the Measurement Matrix H shown in Equation 3.6.

$$\boldsymbol{H} = \begin{bmatrix} \mathbf{0} & \mathbf{0} & \mathbf{0} & \mathbf{1} & \mathbf{0} & \mathbf{0} & \mathbf{0} & \mathbf{0} & \mathbf{0} & \mathbf{0} & \mathbf{0} & \mathbf{0} & \mathbf{0} & \mathbf{0} & \mathbf{0} \\ \mathbf{0} & \mathbf{0} & \mathbf{0} & \mathbf{0} & \mathbf{1} & \mathbf{0} & \mathbf{0} & \mathbf{0} & \mathbf{0} & \mathbf{0} & \mathbf{0} & \mathbf{0} & \mathbf{0} & \mathbf{0} & \mathbf{0} \\ \mathbf{0} & \mathbf{0} & \mathbf{0} & \mathbf{0} & \mathbf{0} & \mathbf{1} & \mathbf{0} & \mathbf{0} & \mathbf{0} & \mathbf{0} & \mathbf{0} & \mathbf{0} & \mathbf{0} & \mathbf{0} & \mathbf{0} \end{bmatrix} \tag{3.6}$$

Since the motion of the foot at that time ZUPT should be 0 the covariance matrix for the update reflects the confidence that the ZUPT is being applied at the correct time and is shown in Equation 3.7. The covariance of 0.1 is used based on the confidence of the step detection algorithms ability to detect the stance phase.

$$\boldsymbol{\sigma^2_{ZUPT}} = \begin{bmatrix} \mathbf{0.1^2} & \mathbf{0} & \mathbf{0} \\ \mathbf{0} & \mathbf{0.1^2} & \mathbf{0} \\ \mathbf{0} & \mathbf{0} & \mathbf{0.1^2} \end{bmatrix} \tag{3.7}$$

3.5 Dual IMU PDR

The dual IMU PDR system is implemented and evaluated using a two-build approach. First is a Dual IMU PDR build, which is a modification to the single IMU system. The system states used by the KF are updated to include both IMUs in the STK. Second is a build that furthers the Dual IMU PDR build with the inclusion of a measurement between the two IMUs, provided by the magnetic sensor. We discuss these two dual IMU PDR system in the following sections.

3.5.1 Build 1: Dual IMU PDR with ZUPT

The ZUPT only variation of the dual IMU PDR system in essence doubles up on the system described in Section 3.4. Meaning the same IMU model that is used in the single IMU PDR system described in Section 3.7.1 and the same Pinson 15 model described previously in Section 3.3.1 that was used in the single IMU PDR is used for each IMU in the system. The high-level data flow of how the two IMU systems

interact with the Scorpion software is shown in block Diagram shown in Figure 4.

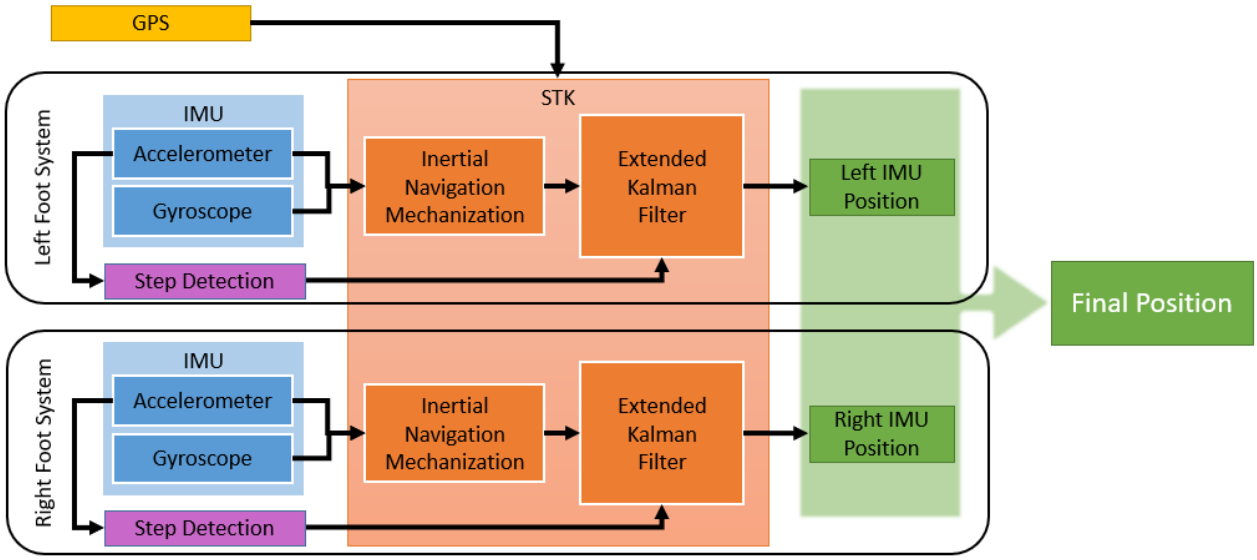

Figure 4: Block Diagram of the dual IMU systems

The filter is designed such that the states for the IMUs on the right and left feet create two independent 15×1 state vectors shown in Equation 3.8.

$$\begin{aligned} \boldsymbol{x}_{right} &= \begin{bmatrix} \boldsymbol{\delta p}_{right} & \boldsymbol{\delta v}_{right} & \boldsymbol{\delta \phi}_{right} & \boldsymbol{\delta b}_{\boldsymbol{a}right} & \boldsymbol{\delta b}_{\boldsymbol{g}_{right}} \end{bmatrix}^T \\ \boldsymbol{x}_{left} &= \begin{bmatrix} \boldsymbol{\delta p}_{left} & \boldsymbol{\delta v}_{left} & \boldsymbol{\delta \phi}_{left} & \boldsymbol{\delta b}_{\boldsymbol{a}left} & \boldsymbol{\delta b}_{\boldsymbol{g}_{left}} \end{bmatrix}^T \end{aligned} \tag{3.8}$$

Using the independent state vectors shown above, the STK forms the system dynamics creating a set of Pinson 15 models for the right and left IMUs. STK is also used to propagate and update independently or be combined diagonally into a 30×30 as shown in Equation 3.9.

$$\boldsymbol{F} = \begin{bmatrix} \boldsymbol{F}_{right} & \boldsymbol{0}_{15\times15} \\ \boldsymbol{0}_{15\times15} & \boldsymbol{F}_{left} \end{bmatrix} \tag{3.9}$$

The Dual IMU ZUPT application for the left and Right IMUs is calculated in-

dependent of each other. The updates for the filter are then applied to the velocity states in the Pinson model independently through the Measurement Matrix H shown in Equation 3.10 and Equation 3.11. The ZUPTs that are applied both utilize the same covariance matrix shown in Equation 3.7.

$$\boldsymbol{H_{right}} = \begin{bmatrix} \mathbf{0}_{3\times3} & \boldsymbol{I}_{3\times3} & \mathbf{0}_{3\times3} & \mathbf{0}_{3\times3} & \mathbf{0}_{3\times3} & \mathbf{0}_{3\times3} & \mathbf{0}_{3\times3} & \mathbf{0}_{3\times3} & \mathbf{0}_{3\times3} & \mathbf{0}_{3\times3} \end{bmatrix}_{3\times30} \tag{3.10}$$

$$\boldsymbol{H_{left}} = \begin{bmatrix} \mathbf{0}_{3\times3} & \mathbf{0}_{3\times3} & \mathbf{0}_{3\times3} & \mathbf{0}_{3\times3} & \mathbf{0}_{3\times3} & \mathbf{0}_{3\times3} & \boldsymbol{I}_{3\times3} & \mathbf{0}_{3\times3} & \mathbf{0}_{3\times3} & \mathbf{0}_{3\times3} \end{bmatrix}_{3\times30} \tag{3.11}$$

3.5.2 Build 2: Dual IMU PDR with magnetic ranging measurement

As mentioned previously mentioned in Section 3.5, the second variation of the dual IMU takes the filter designed in Section 3.5.1 and incorporates a relative position update from the magnetic sensors. Figure 5 is a top-level block diagram identifying how the Magnetic sensors are implemented in the overall system. How the relative position measurement from the magnetic sensors is designed and implemented in the Scorpion software is outlined in Section 3.5.2.1.

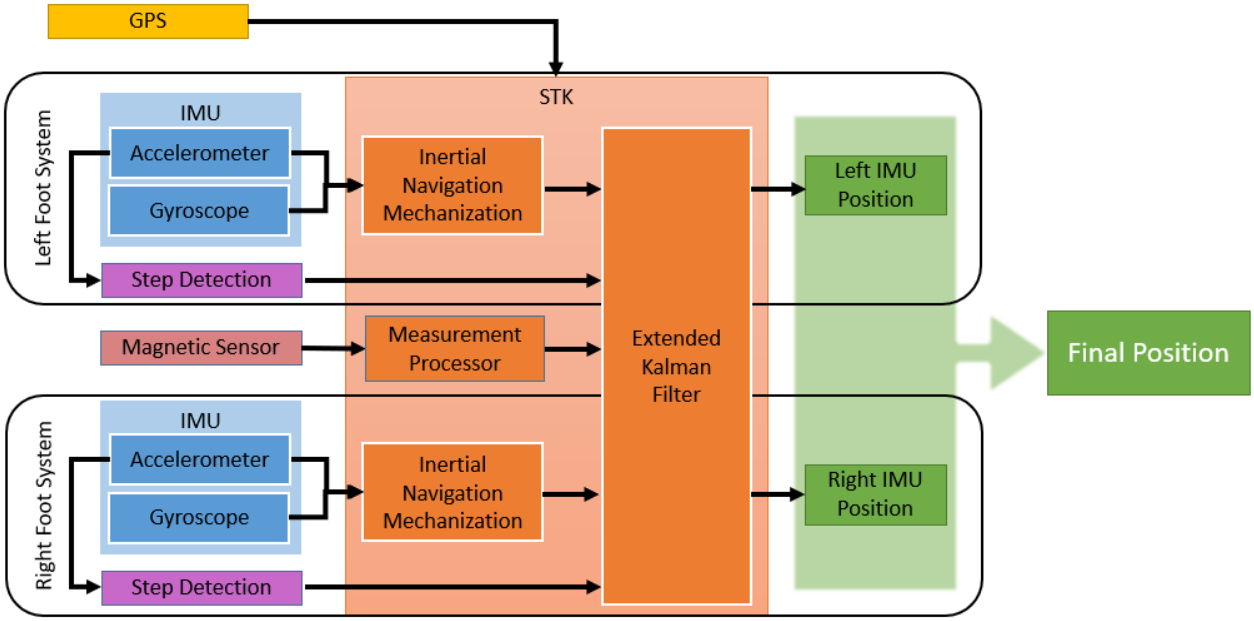

Figure 5: Block Diagram of the dual IMU systems with relative magnetic ranging measurement

3.5.2.1 Magnetic Position Update

For the magnetic ranging measurement between the two feet, the difference in latitude, longitude, and alt from the left and right IMU is computed and converted to meters through the Scorpion Toolkit.

The right and left IMUs are updated given by the measurement matrix equations from Equation 3.12 through Equation 3.13 where the δp is the distance between the two magnetic sensors.

$$\boldsymbol{H}_{Right} = \frac{1}{\|p_{right} - p_{left}\|} \begin{bmatrix} \boldsymbol{\delta p_x} & \boldsymbol{\delta p_y} & \boldsymbol{\delta p_z} & 0 & 0 & 0 & 0 & 0 & 0 & 0 & 0 & 0 & 0 & 0 & 0 \end{bmatrix} \tag{3.12}$$

$$\boldsymbol{H}_{left} = \frac{1}{\left\|p_{right} - p_{left}\right\|} \begin{bmatrix} -\boldsymbol{\delta p_x} & -\boldsymbol{\delta p_y} & -\boldsymbol{\delta p_z} & \mathbf{0} & \mathbf{0} & \mathbf{0} & \mathbf{0} & \mathbf{0} & \mathbf{0} & \mathbf{0} & \mathbf{0} & \mathbf{0} & \mathbf{0} & \mathbf{0} & \mathbf{0} \end{bmatrix} \tag{3.13}$$

The left and right measurement matrices are then concatenated and applied the the 30×30 system dynamics matrix.

$$\boldsymbol{H} = \begin{bmatrix} \boldsymbol{H}_{right} & \boldsymbol{H}_{left} \end{bmatrix}_{1\times 30} \tag{3.14}$$

We estimate the range from sensor to source to be about $1 - 2$ meters, so from Figure 7, we estimate a covariance of 0.001 meters on both sensors. Because the measurement is the difference of the two independent location measurements, the total covariance on the measurement will be 0.002, as shown in Equation 3.15

$$\sigma^2 = \begin{bmatrix} \mathbf{.002^2} & \mathbf{0} & \mathbf{0} \\ \mathbf{0} & \mathbf{.002^2} & \mathbf{0} \\ \mathbf{0} & \mathbf{0} & \mathbf{.002^2} \end{bmatrix} \tag{3.15}$$

3.6 Step Detection Algorithm

There are many ways to accomplish step detection. However, the step detection algorithm chosen for this research is a four-step "batch-mode algorithm" presented in [30]. Their algorithm was chosen because of its versatility. It can use either the data from the accelerometer or the gyroscope to detect steps. This research uses the accelerometer for its step detection because their algorithm provides a 0.1% detection error when using the accelerations measurements versus 0.2% detection error when utilizing the gyroscope data for step detection. For completeness, the algorithm is described below. Note that this algorithm assumes a "sample window" consisting of

20 samples from the accelerometer. This algorithm is run on a sliding window of the samples, so each individual sample will actually be analyzed multiple times.

Step 1: The magnitude of the acceleration is computed for every sample

$$a_i = \sqrt{a_{xi}^2 + a_{yi}^2 + a_{zi}^2} \tag{3.16}$$

Step 2: Local acceleration variance is computed as shown in Equation 3.17 with $\overline{a_j}$ representing the mean of the acceleration magnitudes in the sample window, and is computed as shown in Equation 3.18. w represents a sample window and is the same for both Equations.

$$\sigma_{ai}^2 = \frac{1}{2w+1} \sum_{j=i-w}^{i+w} (a_j - \overline{a_j})^2 \tag{3.17}$$

$$\overline{a_j} = \frac{1}{2w+1} \sum_{q=i-w}^{i+w} (a_q) \tag{3.18}$$

,

Step 3: The swing and stance phases are identified by evaluating σ_{ai} against a predetermined threshold value. The swing phase identification or $B1$ is calculated by Equations 3.19 given that a threshold of ($T1 = 2m/s^2$) is set. Likewise, a threshold of ($T2 = 1m/s^2$) is set to detect the stance phase or $B2$ computed according the Equation 3.20.

$$B1_i = \begin{cases} T1 & \sigma_{ai} > T1 \\ 0 & else \end{cases} \tag{3.19}$$

$$B2_i = \begin{cases} T2 & \sigma_{ai} < T2 \\ 0 & else \end{cases} \tag{3.20}$$

Step 4: Finally, steps can then be identified given there is a transition from a swing to the stance phase. Two conditions must be met independently for the detection of a step to occur:

- The current swing identification $B1_i$ at time i is less than the previous swing identification value $B1_{i-1}$
- There is least one stance phase identified within the window w ahead of the current sample *i.e.*, $max(B2_{i:i+w}) = T2$

3.7 Equipment Overview

For this thesis several pieces of equipment are used to collect the data that is analyzed in addition to the software used. The following sub sections outline each of the pieces of equipment and how they are connected to each other.

3.7.1 IMU

The IMU used for both the single IMU and the dual IMU PDR systems is the Analog Devices, Inc. ADIS16470 IMU shown in Figure 6. The data sheet [31] for the ADIS16470 describes it as a miniature Micro-electromechanical Systems (MEMS) IMU which houses a gyroscope and accelerometer that provide triaxial measurements.

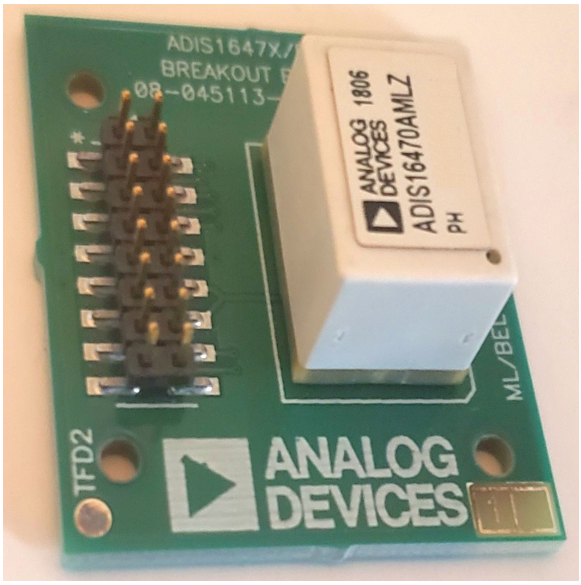

Figure 6: Image of the Sensor Assembly

The specifications listed in Table 1 are gathered from [32]. The testing done in [32] has taken a a set of the ADIS16470 IMUs and evaluated a combination of the Allan variance slope method and Autonomous Regression Method for Allan Variance to identify accurate estimates of the sensor noises. These specification are input into the Scorpion framework to create an IMU dynamics model for use in the filter.

Sensor	White Gaussian Noise (WGN)	Random Walk Noise	τ
Accelerometer	$9.5e-4\ \frac{m}{s^2}$	$1.05e-3\ \frac{m}{\sqrt{s^2}}$	$60\ s$
Gyroscope	$7.85398163e-05\ \frac{rad}{s}$	$1.22173048 * 10^{-5}\ \frac{rad}{\sqrt{s}}$	$60\ s$

Table 1: Values used to generate the IMU model

3.7.2 Magnetic Sensors System

To implement a dual IMU system with relative measurements between the two IMUs, we utilized a G4^{TM} system designed by Polhemus.[33] This system is composed of a single magnetic source, a system electronic unit with a wireless USB module, and

a pair of Micro Sensor 1.8$^{\text{TM}}$s that are rigidly attached close to the IMUs. A brief description of each of the components is discussed individually later in this section. As stated in the Polhemus G4$^{\text{TM}}$ manual [34] the system provides a set of Cartesian position coordinates in the form of X, Y, Z and a set of Euler Angles expressing the Azimuth, Elevation, and Roll of the sensor with respect to a defined origin. The Polhemus system can define its origin to be anywhere, but it has to be fixed with respect to the source. We have defined the origin as the magnetic source itself for this thesis. The accuracy of the position and orientation is dependent on the distance from the given source. Figure 7, taken from the G4 product brochure [2], shows the predicted accuracy of the position and orientation estimates as a function of distance from the source.

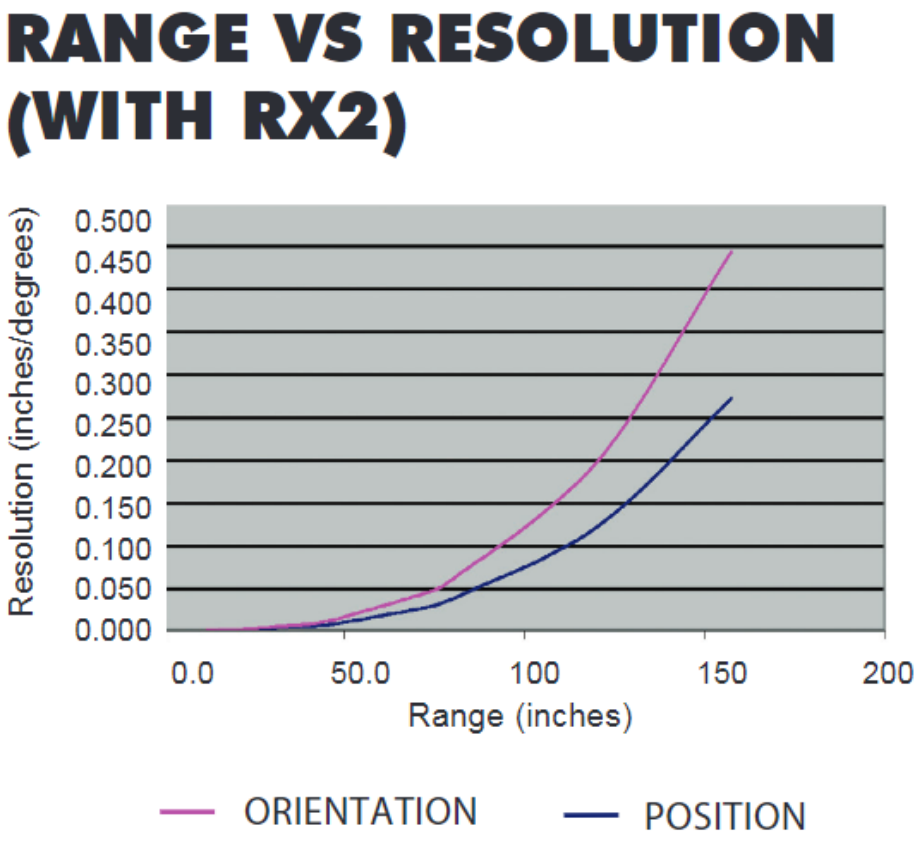

Figure 7: Range vs Resolution chart from the G4^{TM} product brochure [2] (Used with permission from Polhemus)

Magnetic Source: The source shown in Figure 8 is a 4 inch cube that generates the magnetic field which allows the magnetic sensors to determine their location and orientation with respect to the source. [2] The source is configured to be the origin from which each of the Micro Senors measure their relative position and orientation from.

Figure 8: Image of the $4'' \times 4'' \times 4''$ Polhemus G4^{TM}source

System Electronic Unit: The system electronic unit (also referred to as "the hub") is responsible for collecting data from the micro magnetic sensors and calculating the position and orientation of these sensors with respect to the source. A picture of this unit is shown in Figure 9. The hub is connected to a computer or a chosen data recording system via either a direct wired USB connection or through a Bluetooth connection to a USB dongle that is connected to a computer.[34]

Figure 9: Image of the Polhemus G4™ system electronic unit from the G4™product brochure [2](Used with permission from Polhemus)

Micro Sensor 1.8™: These sensors are very light weight and extremely small as shown in Figure 10. They were chosen for this thesis because of their highly desirable size and weight characteristics. Their light weight and small size would make mounting them directly inside a shoe possible (e.g. in a small hole in the sole or between padding layers inside the shoe), making it an ideal sensor for the shoe-mounted PDR application. Despite this small size, the vendor claims excellent accuracy characteristics for this sensor (see Figure 7).

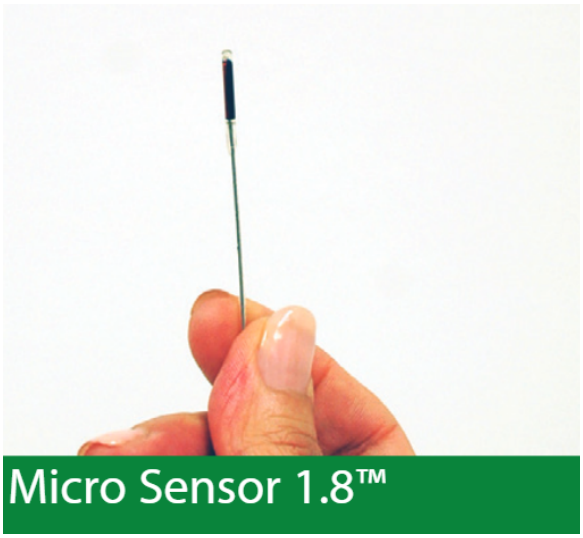

Figure 10: Image of the Polhemus G4™ Micro Sensor™ (Used with permission from Polhemus)

3.7.3 Equipment Setup

Each piece of equipment just described will either be placed on a shoe in what we call the "sensor assembly", or mounted to a backpack to enable easy portage of the larger equipment (the "carry pack assembly"). Additionally the Polhemus system electronics unit which is required doesn't fit into either packages and can be attached anywhere either on the person or the sensor pack. These assemblies are worn by the user as shown in Figure 11 to create the complete PDR system from which the data is gathered. A break down of what is included in each of the carry pack assembly and the sensor assembly is discussed further in Sections 3.7.3.1 and 3.7.3.2.

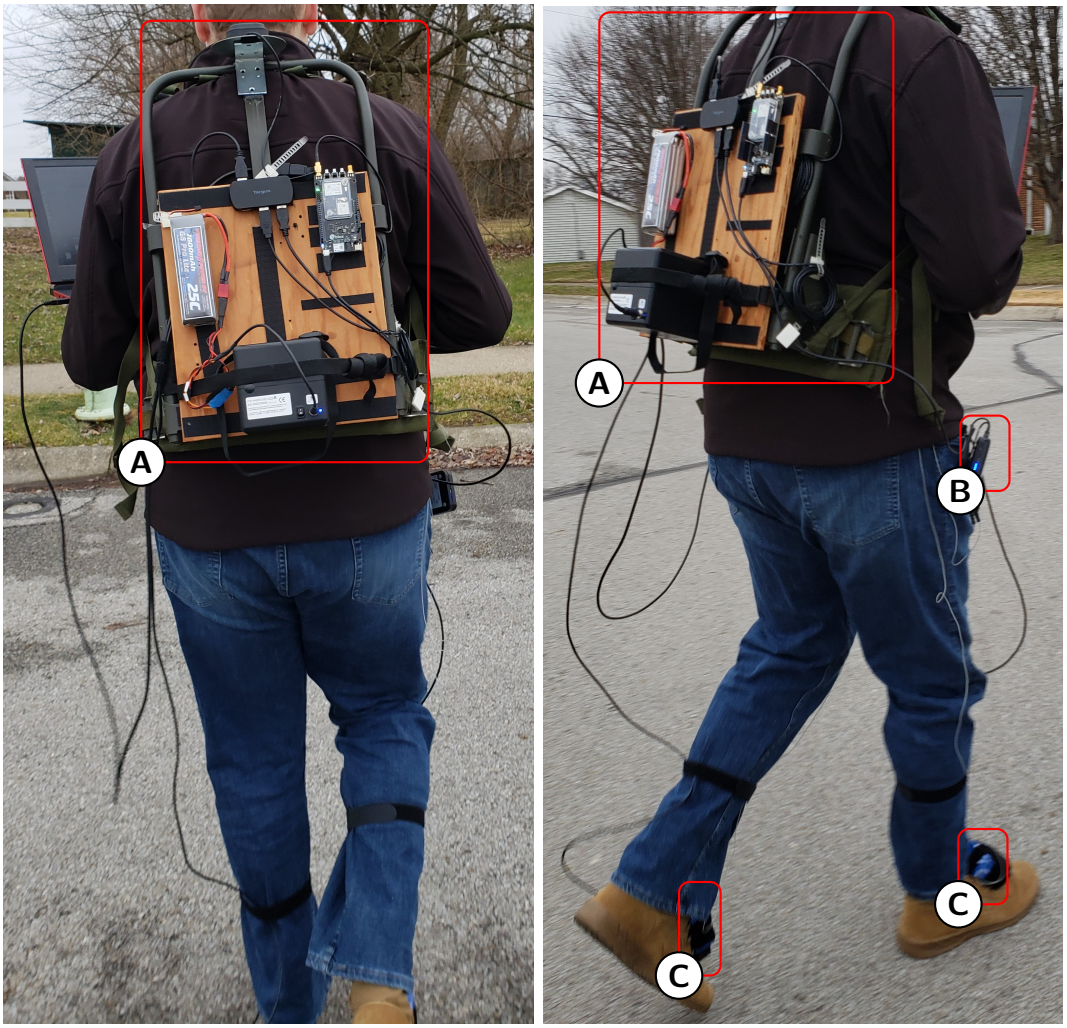

Figure 11: Left:Image of the equipment being worn with the carry pack assembly shown (A); Right: Image of the equipment being worn with the carry pack assembly(A), Polhemus system electronics unit(B) and the sensor assembly(C) visible

3.7.3.1 Carry Pack Assembly

The carry pack assembly is essentially a backpack type system that carries several pieces of vital equipment. The most important piece of equipment mounted is the Polhemus Magnetic Source. The source is mounted to the pack and powered by a LiPo Battery also mounted to the pack. On the top of the carry pack the GPS system

and its antenna mounted for the best reception. This GPS is used for the limited purpose of gathering "truth" data that the single and dual IMU PDR systems are measured against and for system initialization. Lastly there is a USB hub mounted to the pack to enable the Sensor Assemblies, GPS, and Polhemus system electronics unit to all connect to a single port on a laptop for data collection.

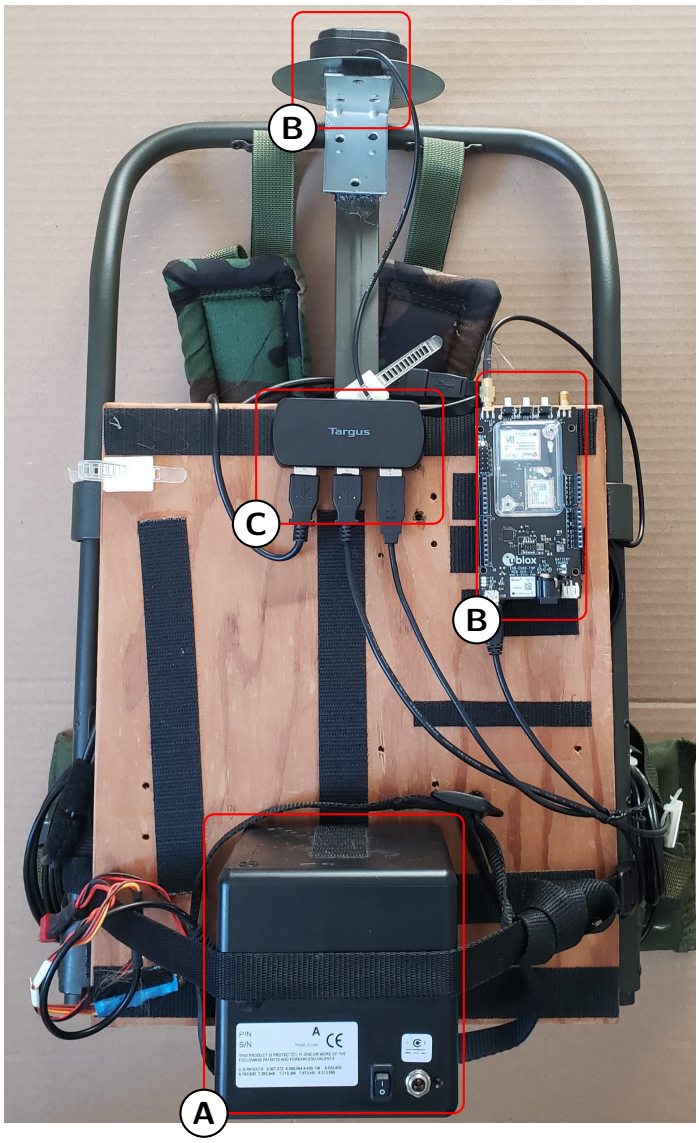

Figure 12: Image of the carry pack assembly: A)Polhemus magnetic source; B) GPS system; C) USB hub

3.7.3.2 Sensor Assembly

The Sensor assembly shown in Figure 11 is packaged in the blue containers attached to the user's feet as shown in Figure 11. The internals of the the sensor pack consist of an ADIS16470 IMUs connected to an Arduino Nano via a 16-pin ribbon cable specially designed for this IMU. The Arduino is responsible for (a) collecting the data from the IMU in a timely fashion, (b) accurately time-stamping the collected data from the IMU, and (c) sending the data to the collecting computer via a serial connection. On the outside of the sensor assembly container one of the Polhemus Micro Sensor^{TM} is mounted in a fixed orientation with respect to the sensor assembly. It is mounted on the outside to reduce any interference with the other equipment in the sensor assembly. The micro sensor cable is run along the leg of the user and connected to the Polhemus system electronic unit. A micro-USB cable is used to connect the IMU and Arduino combo to the USB hub attached to the Carry Pack.

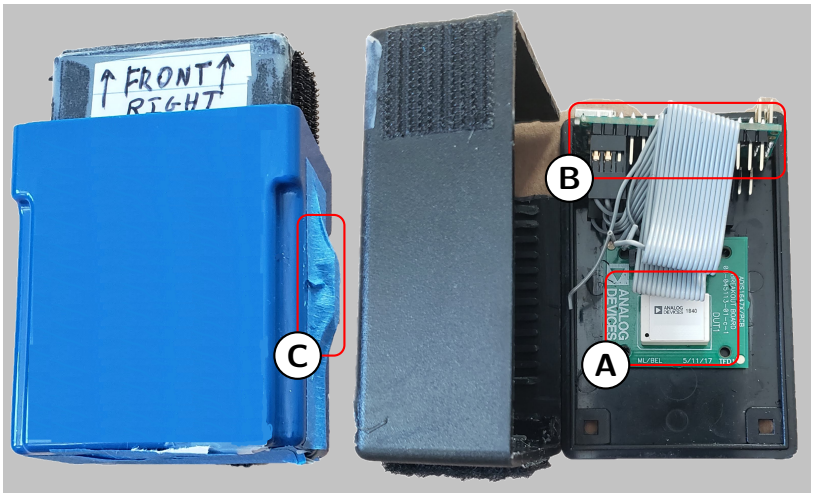

Figure 13: Image of the sensor assembly: A)ADIS16470 IMU; B)Arduino Nano connected by the 16-pin ribbon cable; C)Polhemus Micro Sensor

IV. Results and Analysis

4.1 Overview

This chapter presents results demonstrating the accuracy of the systems introduced in Chapter III. This chapter is organized as follows. Section 4.2 evaluates the accuracy of the proposed step detection algorithm. Section 4.3 describes the data collection scenarios that were used to test the accuracy of our system. Sections 4.4 - 4.7 presents results from the single Inertial Measurement Unit (IMU) Pedestrian Dead Reckoning (PDR), dual IMU PDR, and dual IMU PDR with magnetic sensors systems.

4.2 Step Detection

This section reviews the results of the the step detection algorithm that was presented in [30] and described in Section 3.6. To evaluate the detection algorithm, several tests were conducted in which an average walking pace of approximately 4 MPH (6.44 KPH) was used. These tests included walks in which the number of paces ranged from 25 to 150 steps. The truth data for these tests was determined by manually counting the number of steps taken while walking, with a step defined as the point in which the right foot hit the ground. [30] indicated, this algorithm is able to correctly identify steps taken with a 0.1% error rate. The results of the five tests conducted for this thesis are shown in Table 2 which appear to validate the results of [30]. As expected, every step taken was correctly identified and at no point was there a step identified when one was not taken.

Test #	# Steps Taken	# Steps Detected
1	25	25
2	50	50
3	75	75
4	100	100
5	150	150

Table 2: Step Detection Results

As shown in Figure 14, the step detection algorithm correctly identifies the portions of the step when the foot is not accelerating in any direction. This corresponds very well with when the foot is placed on the ground and not moving, i.e., the zero velocity time.

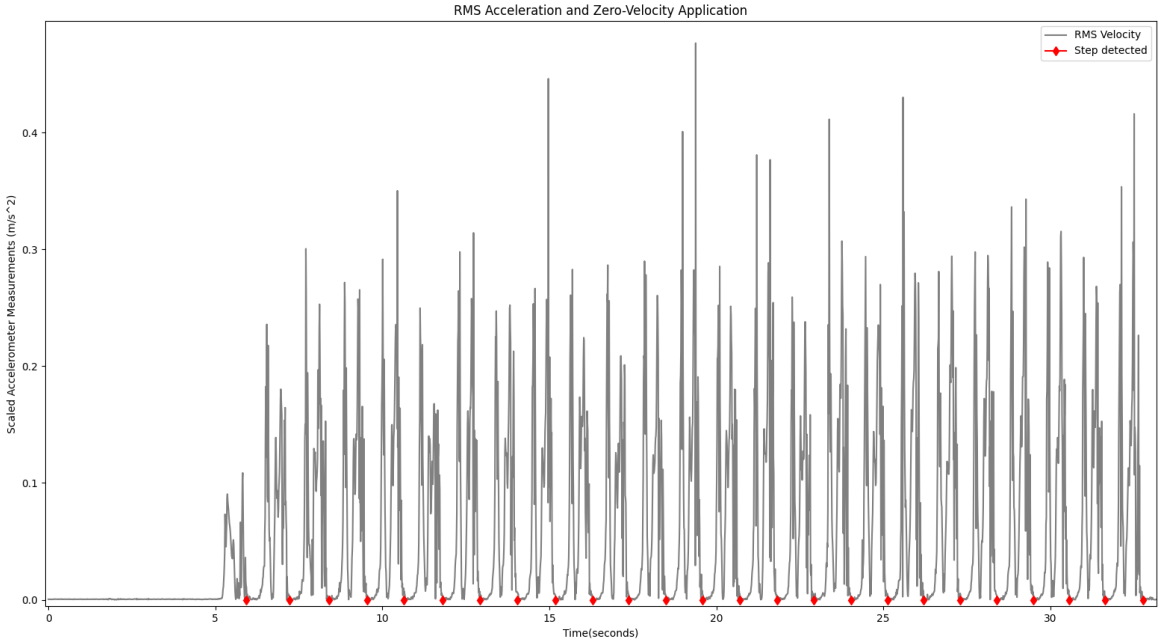

Figure 14: Plot of scaled acceleration used for detection and the identification of steps shown by the red diamonds over a 25 step walk

4.3 Testing Scenarios

Recall from Section 3.2 three different scenarios to test the PDR systems. The first scenario involves walking a single lap around a track with the second scenario encompassing a two-lap walk around the same track. The third scenario is composed of taking a walk through a residential area to test the system's ability to track multiple turns in different directions. The truth data outlining the trajectories for the three scenarios can be seen in Figure 15 and Figure 16.

For each of the scenarios, there is a 150 second initialization period, during which time several "figure 8s" are walked while also providing Global Positioning System (GPS) positioning updates to the filter to reduce the overall IMU biases. The results of the single IMU PDR, Dual IMU PDR with Zero Velocity Update (ZUPT) only, and Dual IMU PDR with ZUPT and magnetic sensors are compared to determine the overall accuracy of each technique. This comparison is done using final position error, error plots of the different PDR systems outlined, and visually comparing the overall trajectories with the truth data that is collected.

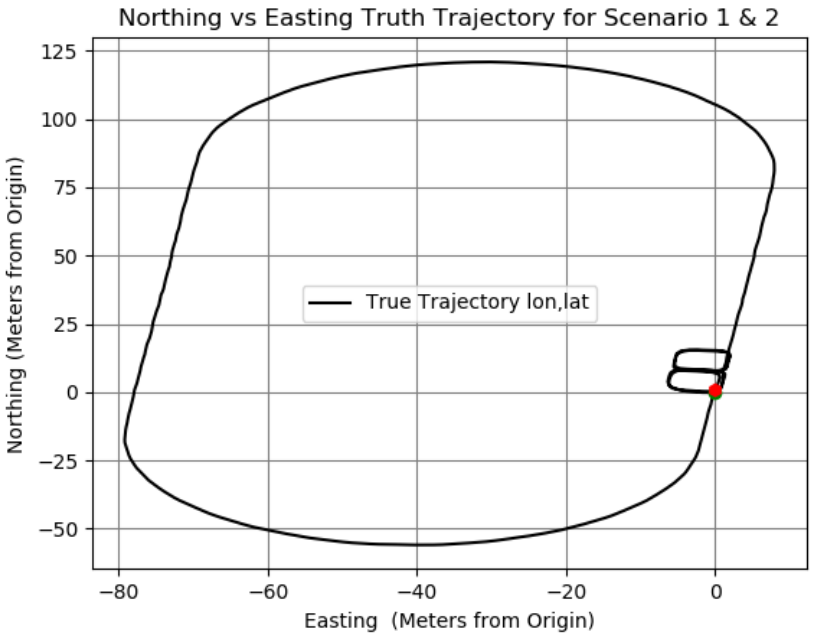

Figure 15: Truth trajectory for the track based scenario 1 and scenario 2

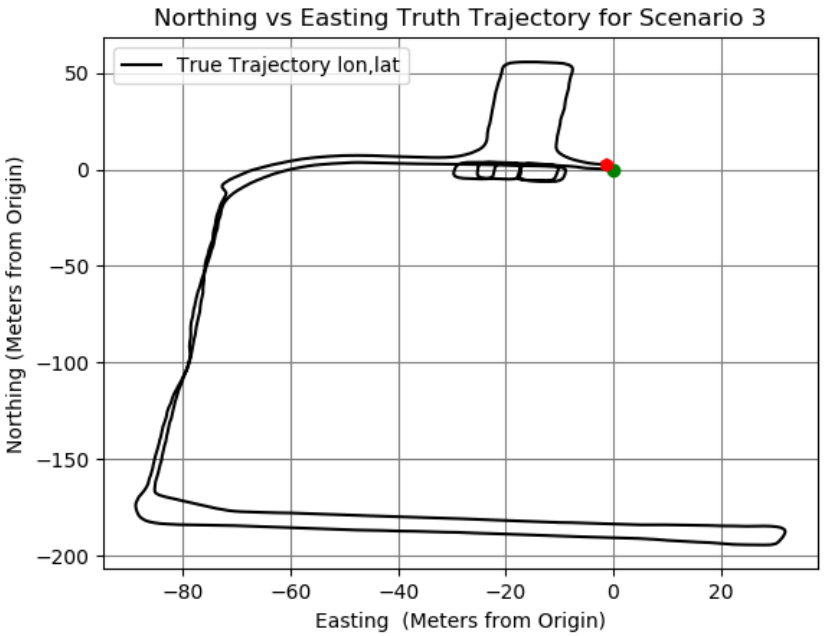

Figure 16: Truth trajectory for the residential walk based scenario 3

4.4 Analysis

The initial interpretation of how the data from the three scenarios performed is outlined in this section with more in-depth discussions on how each of the PDR systems performed in the following sections. As the first set of data from the single lap scenario was evaluated using the single IMU PDR system there were noticeable issues that could be seen shown in Figure 17.

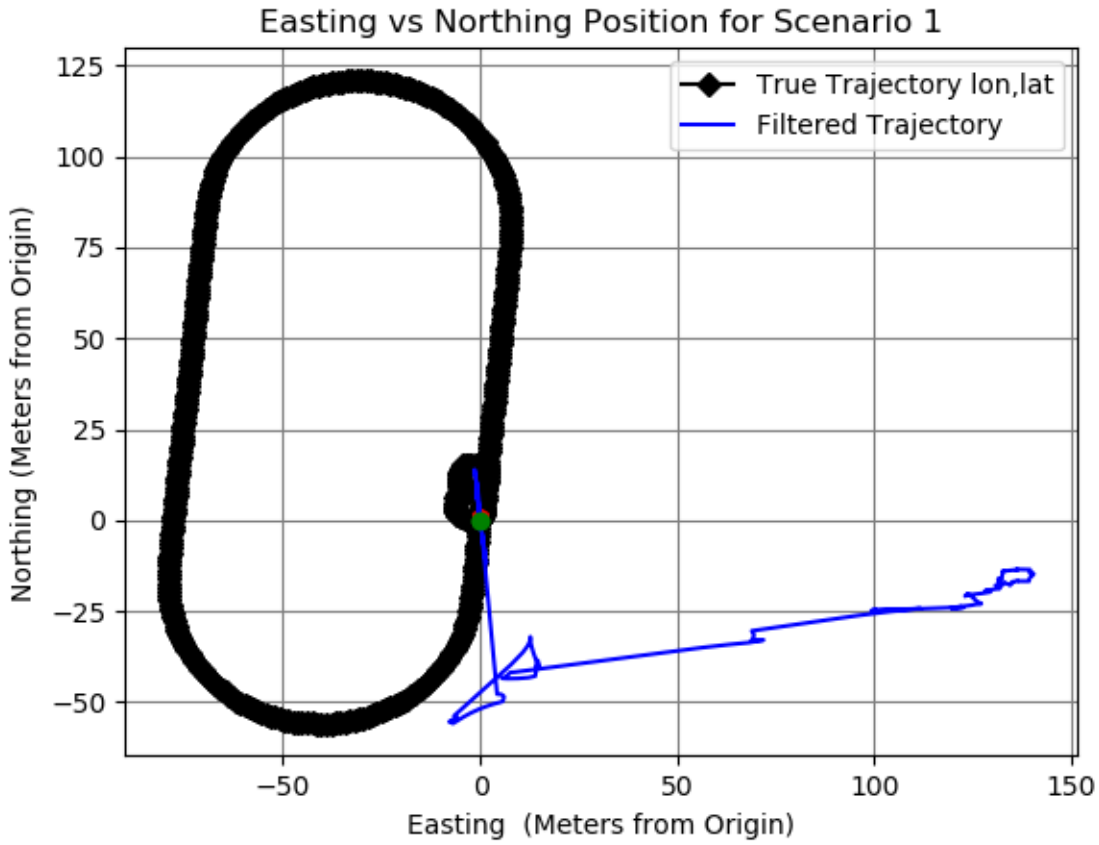

Figure 17: Northing vs Easting trajectory results from test 1 of single IMU PDR System using data from scenario 1

To ensure it was not a set of bad data, multiple collections with the same basic walking pattern were performed. Each collection had similar performance as shown

in Figure 18, pointing us to different sources of error than the data itself.

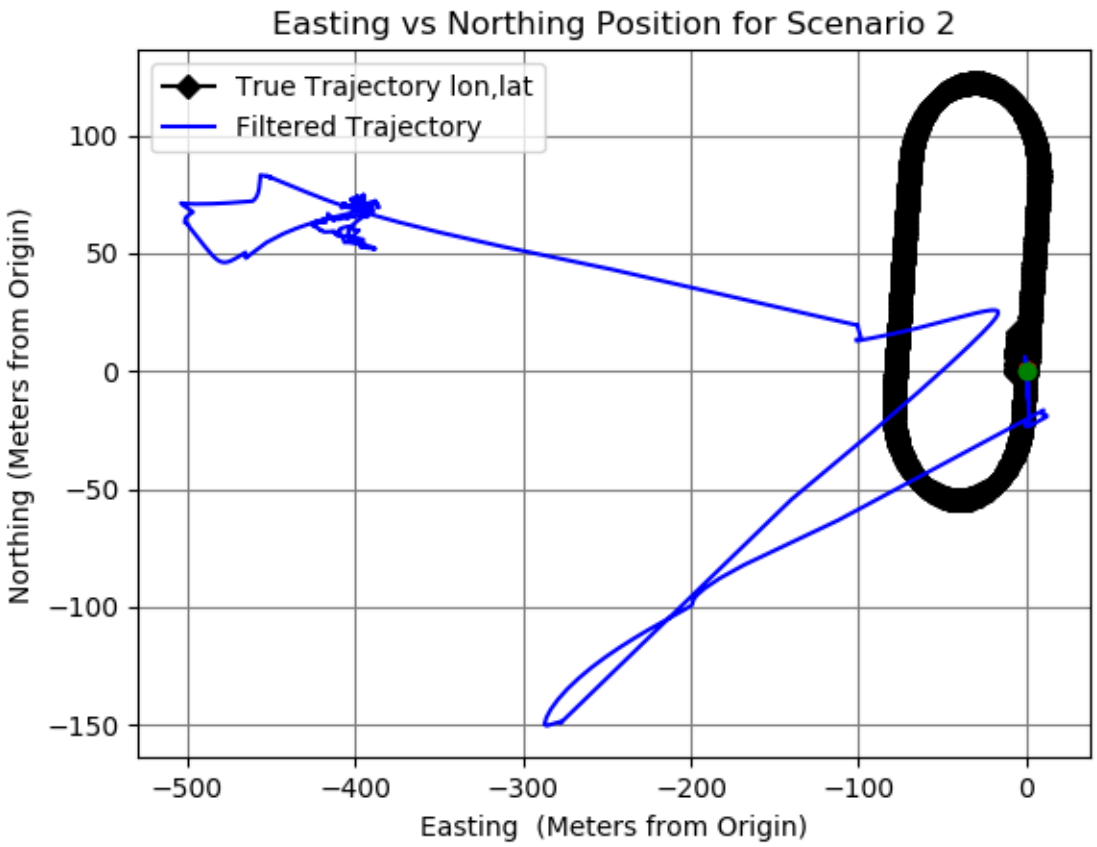

Figure 18: Northing vs Easting trajectory results from test 2 of single IMU PDR System using data from scenario 2

One possible source of these errors could be the tuning of the noise values for the IMU. To test this theory, we reran Scorpion Development Toolkit (STK) on the same data, but with multiplicative tuning values for the gyroscope and accelerometer model. The tuning values were incrementally increased and for each increase the system was rerunning evaluating the ending position error.

The tuning values that performed the best are shown in Table 3 with the results of this tuning shown in Figure 19 and Figure 20. These new IMU model values are

used in the evaluation of the single IMU PDR and the dual IMU PDR systems in the following sections.

Accel Bias	Accel Random Walk	Gyros Bias	Gyro Random Walk
35	350	45	450

Table 3: Scale factors used for tuning the IMU model in the STK software

4.5 Single IMU PDR

This section evaluates the single IMU PDR system using the scenarios described in Section 4.3. Table 4 outlines the overall performance of the single IMU PDR system for the three test scenarios be comparing the ending error magnitude, which is followed by the analysis of each scenario.

Test Scenario #	Run length	Initialization Time	Largest Position Error	Final Position Error
1	470.62(s)	150(s)	12.85(m)	9.89(m)
2	826.17(s)	150(s)	39.63(m)	27.38(m)
3	808.51(s)	150(s)	87.96(m)	55.61(m)

Table 4: Results of the Single IMU PDR system

4.5.1 Scenario 1

In Scenario 1, the single IMU PDRsystem performed similar to the other researchers single IMU PDR system described in 2.7.1. The PDR solution shown in Figure 19 follows the true trajectory almost through the first turn. The single IMU solution starts to suffer from heading drift because the filtered solution relies purely on navigation by inertial measurements. The overall system drift is reduced due to the ZUPT measurements. At the filter's worst point, the error is approximately 12.85 meters off from the truth. However, as listed in Table 4 the final ending point is 9.89 meters from the true endpoint.

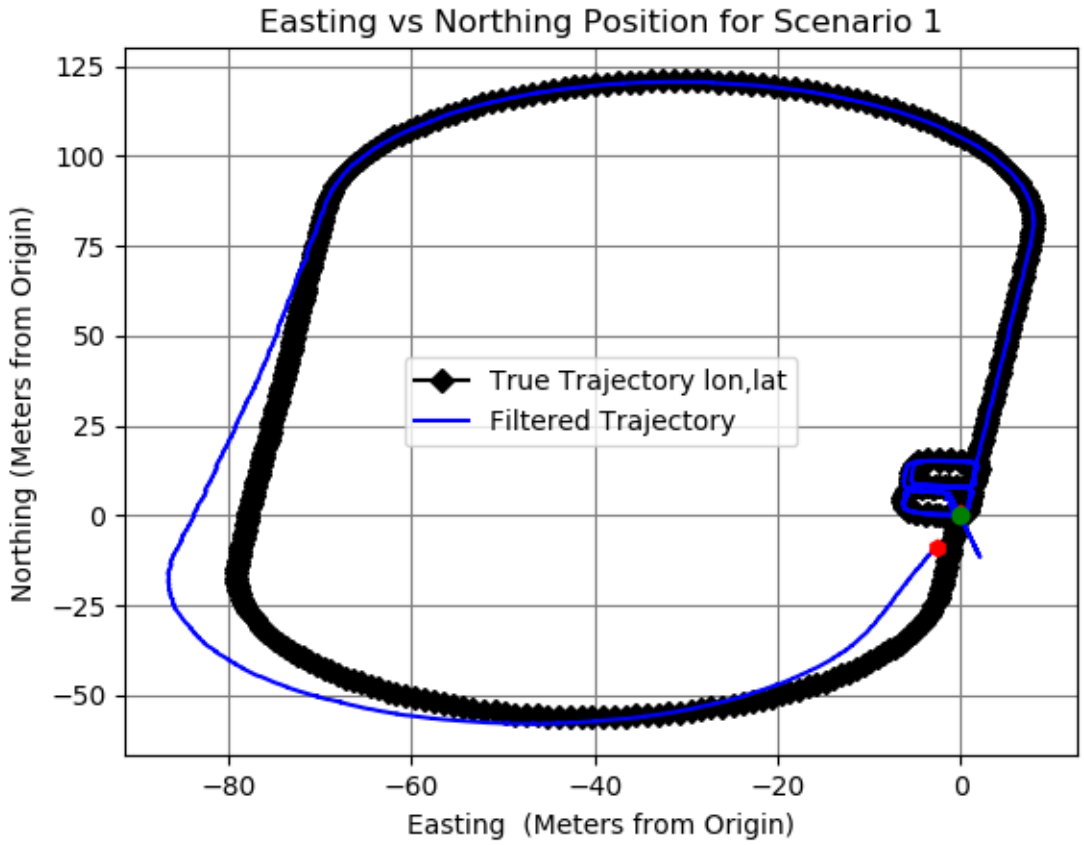

Figure 19: Scenario 1 Northing vs Easting Trajectory for the Single IMU PDR System

4.5.2 Scenario 2

The single IMU PDRfilter system performed as expected with the data set from scenario 2. This scenario's total length is almost double that of the first scenario, and the heading drift becomes more apparent. For this scenario, the Filter solution roughly maintained the same oval shape as the truth. However, the oval shape "rotates" over time because of heading drift. After completing the first lap, the filter solution is almost 10 meters off the true trajectory. The remaining lap around the track leads to an ending position error of 27.38 meters as mentioned in Table 4. Despite this scenario being a little more than 2 times the first scenario's run length, its

error has increased 277%.

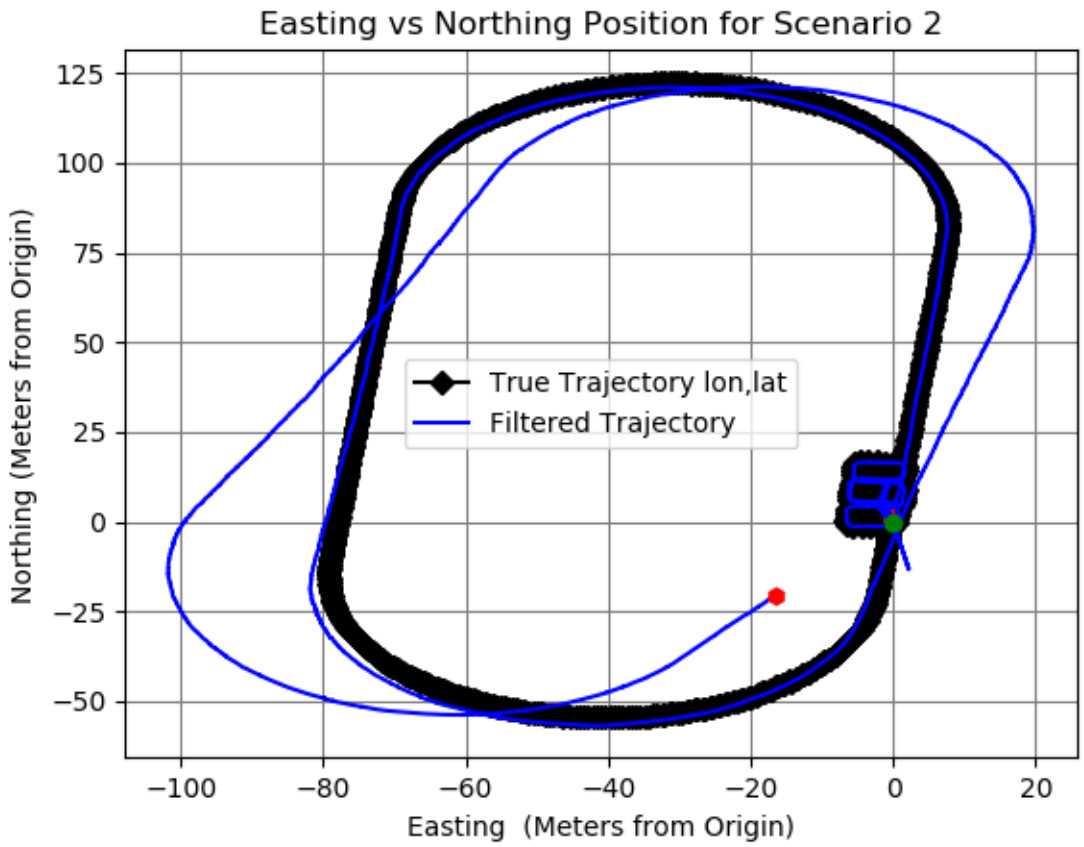

Figure 20: Scenario 2 Northing vs Easting Trajectory for the Single IMU PDR System

4.5.3 Scenario 3

The last scenario identifies how a PDR system would operate when not walking the same pattern multiple times. As expected, the length of the scenario and the number of right and left turns have the largest final position error 55.61 meters. The first thing to note on the trajectory of Scenario 3, shown in Figure 21, is that it appears the heading does not drift very much until the first change in direction after the turnaround. The lack of heading drift could be equated to the drift coinciding with the actual trajectory. A second possibility for the lack of heading drift could be due

to the initialization the filter could maintain a better "lock" on the actual trajectory. Once it does start to drift off toward the east, it can still track the overall shape of the path taken. This scenario underscores the importance of utilizing additional sensors and measurements.

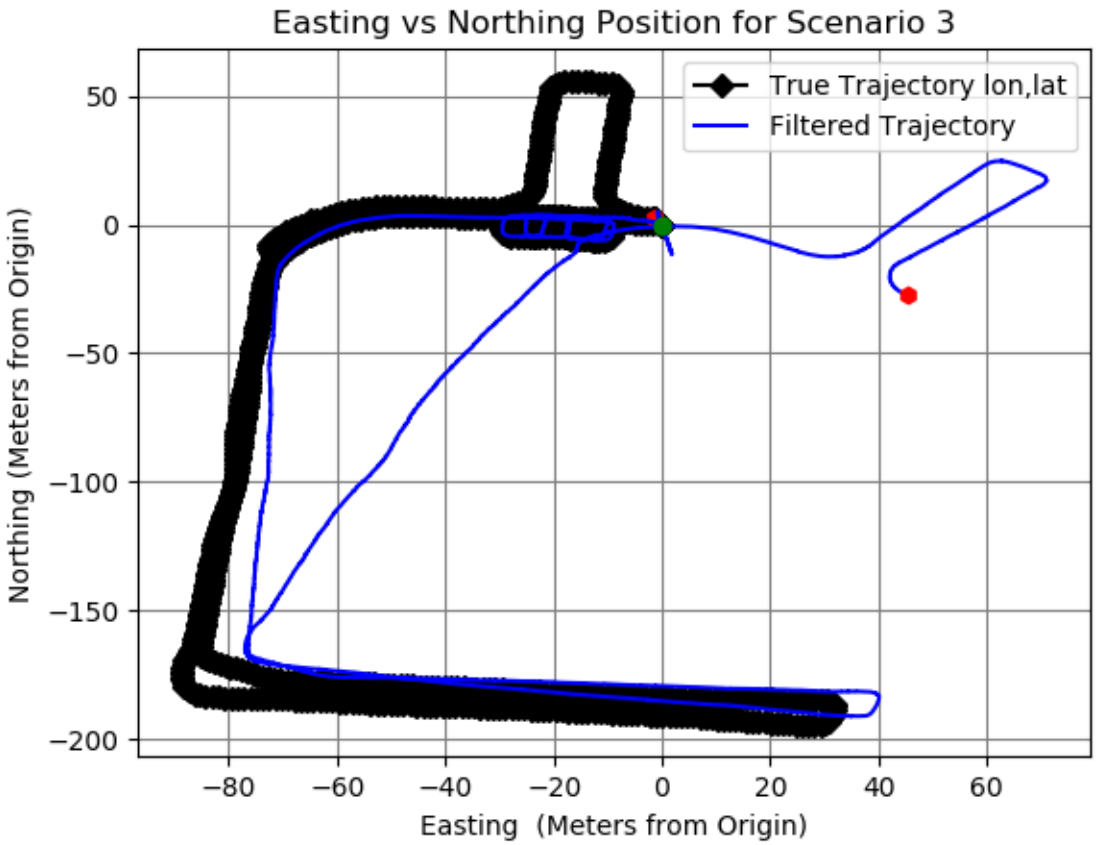

Figure 21: Scenario 3 Northing vs Easting Trajectory for the Single IMU PDR System

4.6 Dual IMU PDR with ZUPT only

Recall from Section 3.5, that the Dual IMU PDR system consists of a sensor assembly on each foot and the positioning results of this system is given by taking the average of two systems. Formatted similarly to the previous section, there is an outline of the Dual IMU PDR system shown below in Table 5. Following this system

results table is an analysis of each scenarios performance.

Scenario	Run length	Initialization Time	Final Position Error L/R IMU	Final Position Error
1	470.62(s)	150(s)	18.98(m)/9.89(m)	4.74(m)
2	826.17(s)	150(s)	52.56(m)/27.38(m)	17.12(m)
3	808.51(s)	150(s)	136.71(m)/55.61(m)	48.58(m)

Table 5: Results of the Dual IMU PDR System using ZUPT only

4.6.1 Scenario 1

Figure 22 shows the Trajectory of the left and right foot Filter solutions along with the final averaged position. The first item of note is how both the left and right foot IMUs drift over time. Each IMU drift is similar to that seen in the single IMU PDR system's IMU in the previous section. The Left and Right IMUs each drift in opposing directions allowing for an evenly weighted average of the two to be computed. As shown earlier in Table 5 the overall averaged position ends with a position error of 4.74 meters after one lap around the track. With the use of two IMUs, the overall position error compared to the Single IMU PDR system is reduced by approximately 52%.

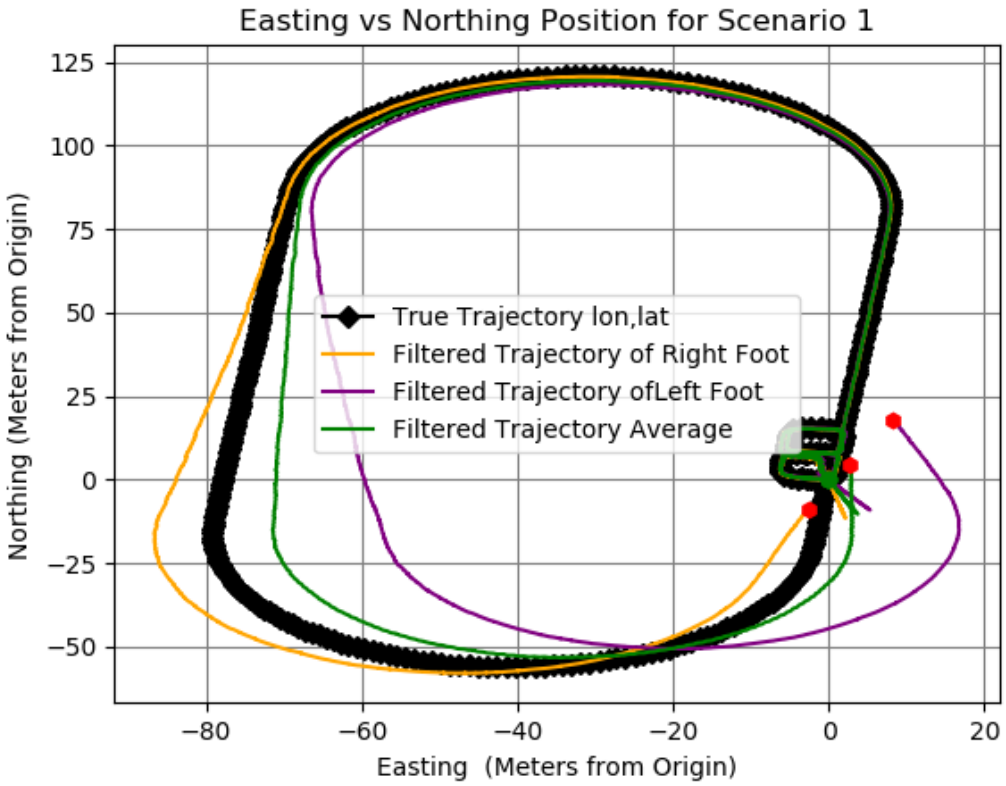

Figure 22: Scenario 1 Northing vs Easting Trajectory for the Dual IMU PDR System using ZUPT Only

From Figure 23 below, showing the break down of the North, East and Down (NED) position, the largest source of error comes from the East-West movement. Between 350 seconds and 450 seconds into the walk the easting error for the IMU on the left foot is greater than 20 meters.

4.6.2 Scenario 2

Similar to the performance of the single IMU PDR PDR, the drift in the IMU heading for both feet is more noticeable in scenario 2. With the two IMU the filtered system had an error of 17.12 meters, which is a 62.53% decrease in error. Like Scenario 1, both the left and right IMUs are off by 20 Meters but on both sides of the truth

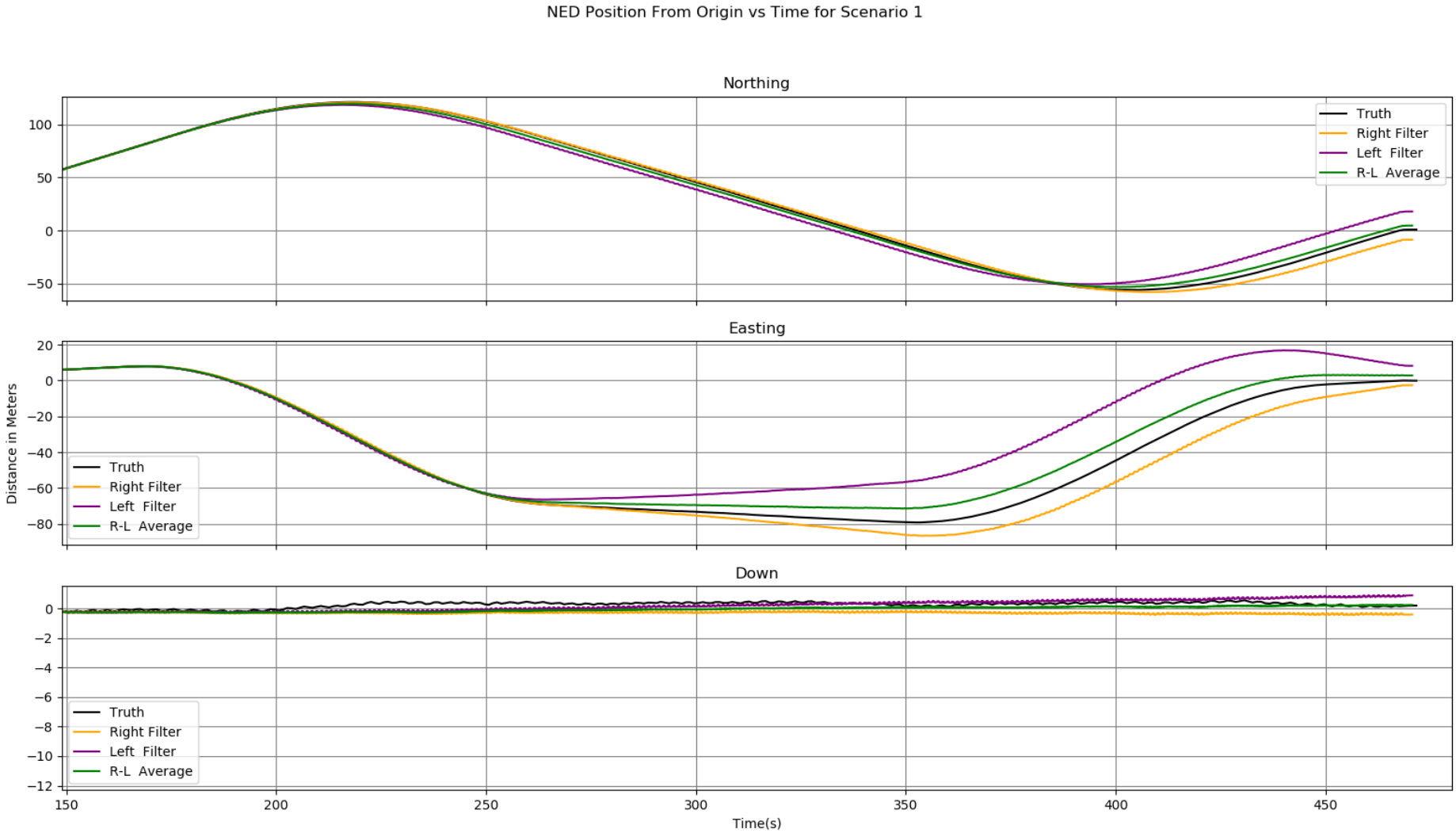

Figure 23: Scenario 1 NED Position Breakout for the Dual IMU PDR System using ZUPT Only

line. By averaging their positions, the accuracy is improved compared to that of the single IMU PDR system.

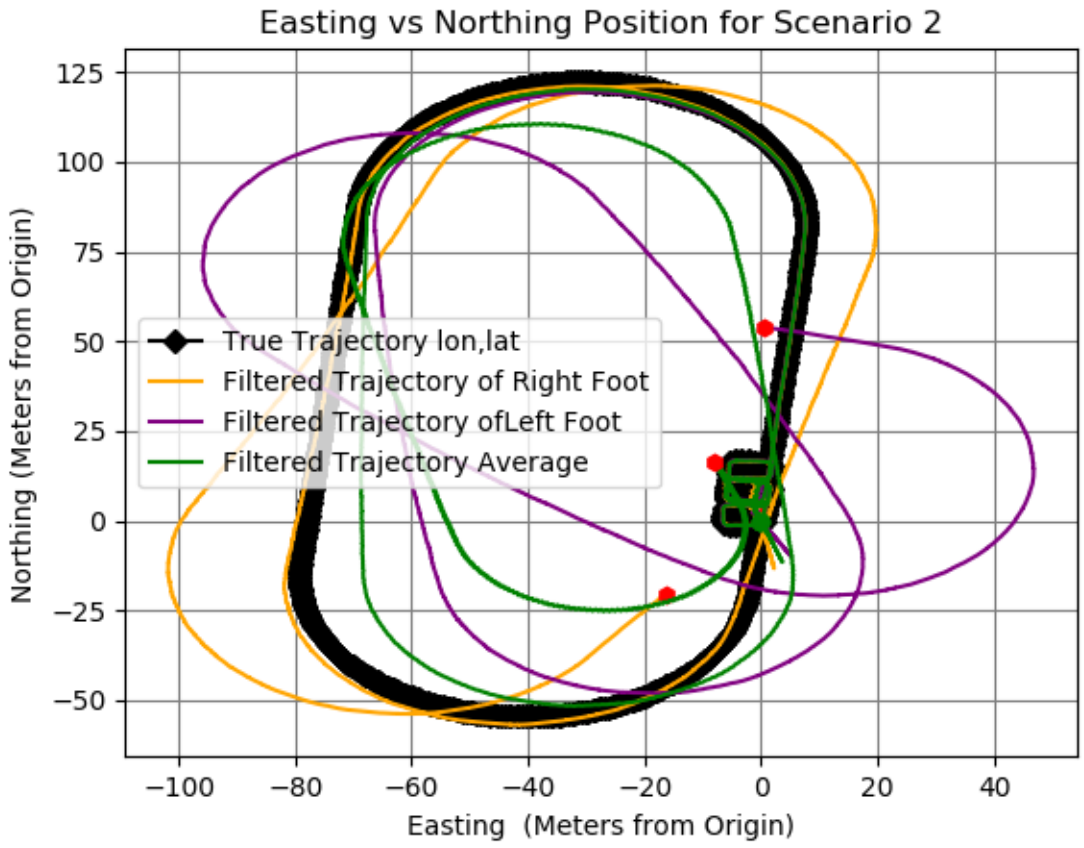

Figure 24: Scenario 2 Northing vs Easting Trajectory for the Dual IMU PDR System using ZUPT Only

4.6.3 Scenario 3

When using the Dual IMU PDR system in Scenario 3, the scenario clearly benefits from having a second IMU. By adding the second IMU the position error decreased from 55.61 meters to 48.58 meters which is a 12.6% decrease in error. Which in and of itself does not sound like a significant decrease, however if you were to examine a single IMU system based on the left IMU trajectory it would be a 64% decrease in

overall error. The other items of note are that the left IMU appears to drift more than the right after the u-turn resulting in a position error for that IMU.

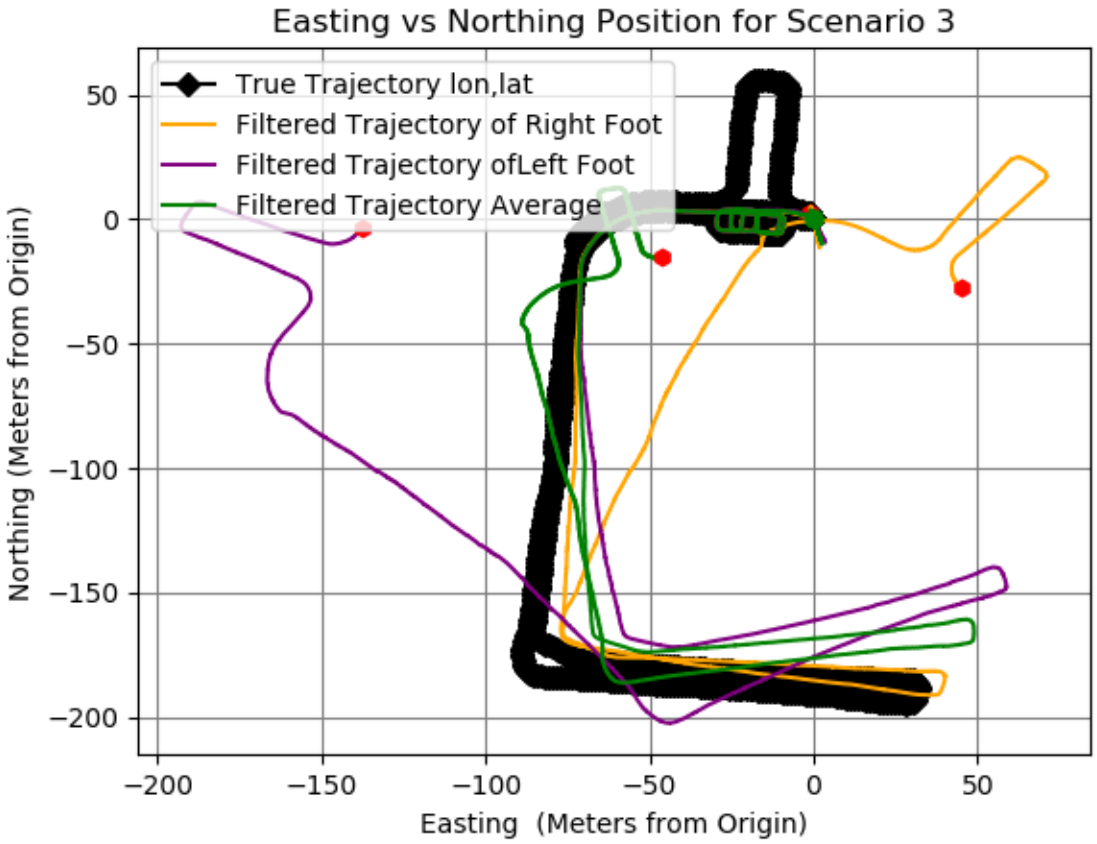

Figure 25: Scenario 3 Northing vs Easting Trajectory for the Dual IMU PDR System using ZUPT Only

4.7 Dual IMU PDR with Foot-to-Foot Ranging

This section looks at the data from the magnetic sensors and evaluates its feasibility to provide the necessary ranging measurements given a dual IMU PDR system. At first glance, the results from the three scenarios shown in Table 6 would indicate that using this magnetic ranging measurement reduces the performance of the dual IMU PDR system. The results and conclusion on why each scenario appears to have

been negatively impacted are discussed in the following sections. These results impact the trajectory from Scenarios 1 and 3, shown in Figure 26 and Figure 28, and are evaluated in more detail below.

Test Scenario #	Run length	Initialization Time	Final Position Error
1	470.62(s)	150(s)	109.07(m)
2	826.17(s)	150(s)	239.05(m)
3	808.51(s)	150(s)	164.39(m)

Table 6: Results of the Dual IMU PDR System using ZUPT and Foot-to-Foot Magnetic Ranging Measurements

4.7.1 Scenario 1

In Figure 28 the most noticeable difference is that after the first 150 seconds of initialization, it no longer stays on track and leads to the system performing imperfectly. Looking at the magnetic range data, used as the measurements for the filter in Figure 27, there are several indicators that the equipment itself could be the problem.

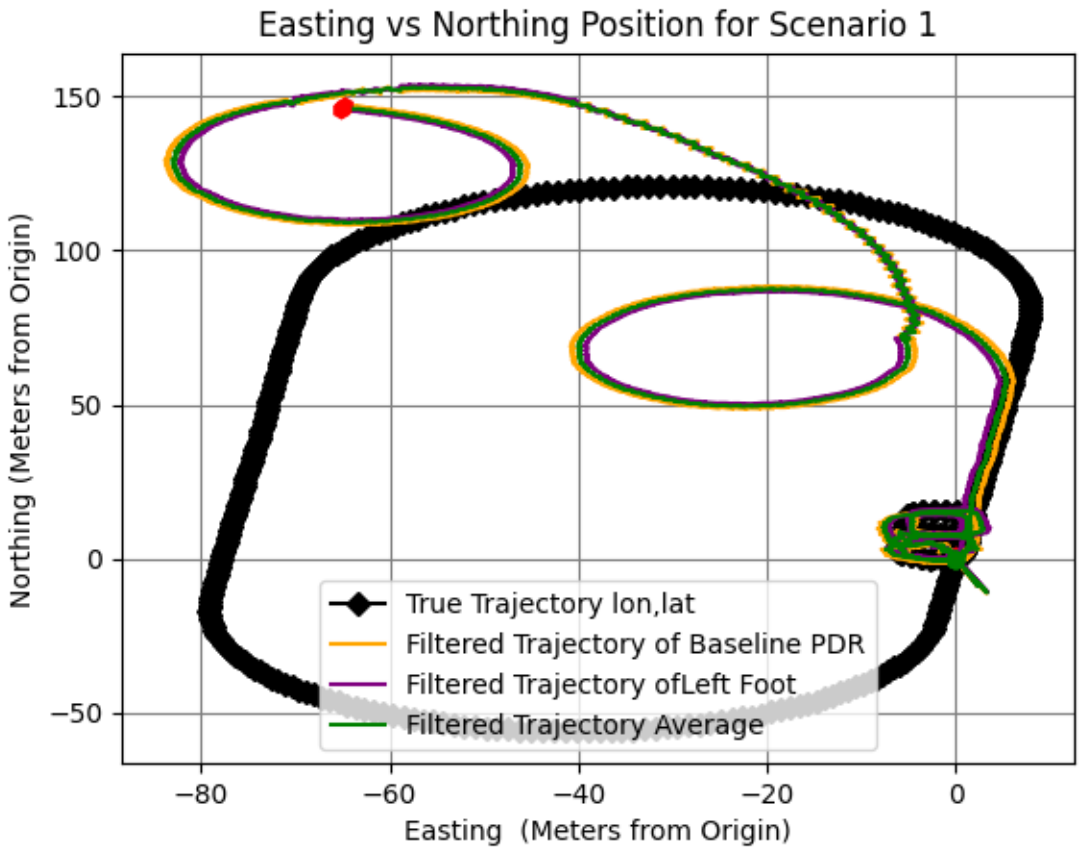

Figure 26: Scenario 1 Northing vs Easting Trajectory for the Dual IMU PDR System using ZUPT and Magnetic Ranging Measurements

Figure 27 shows the raw range measurements coming from the magnetic sensor. These measurements shown indicate that the data provided to the STK was faulty. When walking, no measurement should be more than 1 meter. However, the raw data collected has a max distance of almost 2.5 meters. There is also a fluctuation where some of the measurement averages are around 2.1 meters and other times when it averages around 0.75 meters. The large periods of time during which the foot-to-foot distances does not fall below 1.5 meter confirm our hypothesis that the data given to the STK is the source of error.

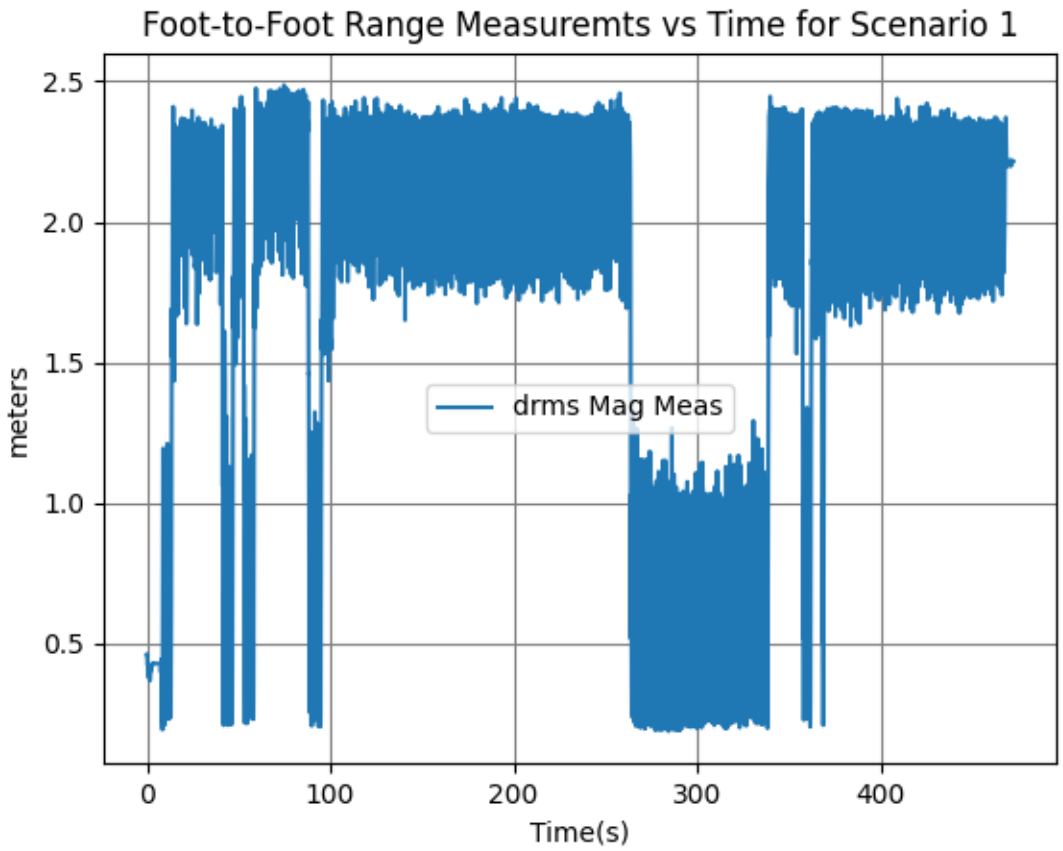

Figure 27: Foot-to-Foot Magnetic Ranging Measurements for Scenario 1

4.7.2 Scenario 3

Similar to Scenario 1, the magnetic ranging measurements did not improve the Dual IMU PDR system performance. In this scenario, instead of pulling the system off the truth trajectory, the measurements keep the system from moving away from the initial position. Similar to the previous scenario, the measurements in this scenario keep the trajectories of the left and right IMU highly correlated. This is indicated in both scenarios by looking at the distance between both the left and right IMUs and noting that the distance does not appear to be any larger than the measurements provided from the magnetic sensors. This leads to a conclusion that if the data was

better, the measurements should decrease the opposing drifts of the left and right IMUs seen in the Dual IMU PDR system in Section 4.6.

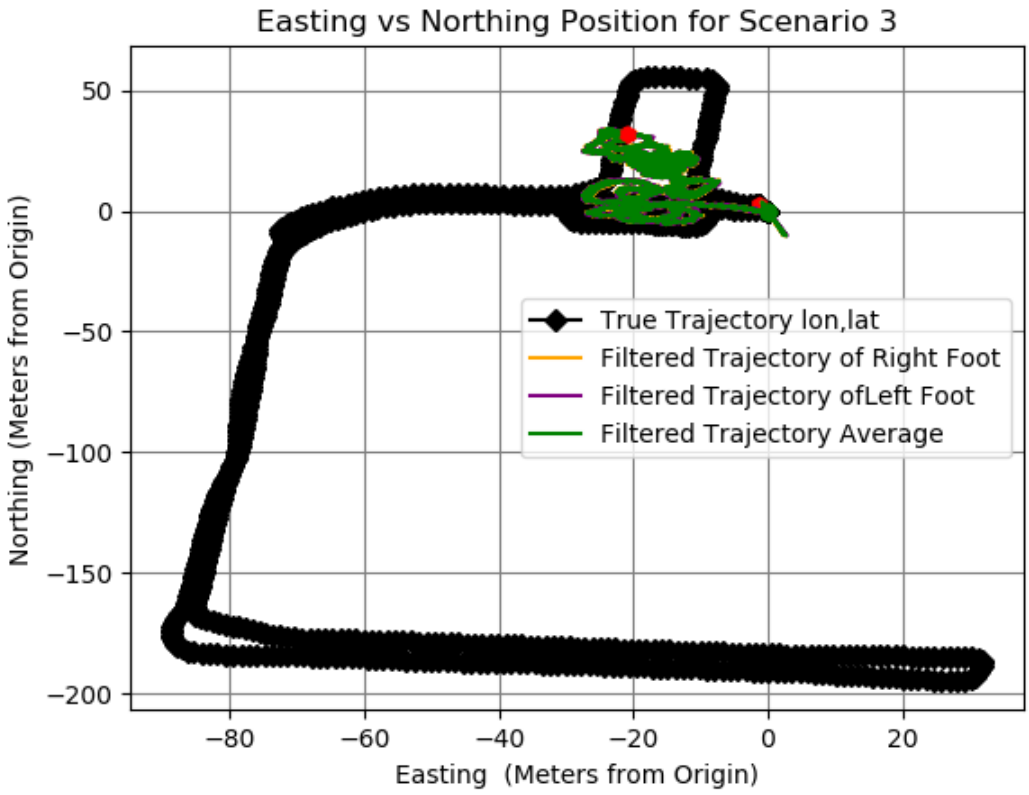

Figure 28: Scenario 3 Northing vs Easting Trajectory for the Dual IMU PDR System using ZUPT and Magnetic Ranging Measurements

There are several potential solutions to achieve better magnetic measurement readings. The first option could be to place the magnetic source closer to the sensors and remove it from the Carry Pack. Another potential solution would be to try a different housing for the IMU to reduce any interference that could corrupt the measurements. The last option available would be to change the magnetic sensors themselves to something a little larger and could potentially provide more consistent readings.

V. Conclusions

5.1 Final Thoughts

The overall purpose of this thesis was to build a testbed to enable Air Force Institute of Technology (AFIT) to evaluate Pedestrian Dead Reckoning (PDR) techniques and sensors. Through the Scorpion Development Toolkit (STK) a PDR testbed was successfully designed. This testbed enabled the evaluation of three foot mounted PDR solutions through the post processing of real-world data. This thesis was able to assess the use of commercial-grade Inertial Measurement Unit (IMU)s while also implementing magnetic sensors ranging measurement.

Through the PDR testbed, the single IMU PDR which utilized a Zero Velocity Update (ZUPT) algorithm and a commercial-grade IMU was evaluated. This evaluation concluded that the single IMU PDR system provided a relatively accurate solution for a short duration. Although the single IMU PDR system loses tracking for longer durations or if multiple turns are taken due to the IMU sensor drift.

The PDR testbed was able to evaluate the the Dual IMU PDR system that utilized a pair of commercial-grade IMUs and the same ZUPT algorithm as the single IMU PDR system. This dual IMU PDR provided improvements over the single IMU PDR system as expected. The improvements in accuracy by utilizing the two IMUs for PDR is quantified with an average of a 60% decrease in position error.

The third system built upon the Dual IMU PDR system with the addition of magnetic sensors providing a foot-to-foot ranging measurement was designed into the testbed but a full evaluation of the system was not possible. Unfortunately, this system did not work as anticipated, given the quality of measurement data itself, which also prevented evaluating the foot-to-foot magnetic ranging system itself.

5.2 Future Work

The research accomplished throughout this thesis provides another starting point for increasing the feasibility of using low-cost systems in a wearable PDR system. As others look to build upon the work done and evaluate other methodologies and sensors, I believe several areas have the potential to provide a considerable benefit to PDR.

5.2.1 Relative Rotation Updates

If the magnetic sensors can be re-positioned to provide more reliable and accurate readings, the relative attitude between the right and left IMU's could be calculated. This form of update could also provide a reduced initialization time or could potentially remove the need for it all together. The inclusion of relative attitude measurements could improve the overall accuracy by reducing some of the heading drift that impacted the Single IMU and Dual IMU systems.

5.2.2 Machine Learning

Given the complex but repetitive motions when walking, jogging, or running and subsequent IMU data captured, several Machine Learning methods have the potential to improve PDR. Several other researchers such as [23],[35], and [36] all have used machine learning to improve the identification of human motion. The aforementioned research and other similar research have shown that Machine Learning could provide improvements. I believe there is a potential that their research in human motion combined with the research done in this thesis could improve the accuracy of PDR.

Bibliography

1. Ed Ayyappa. *Normal human locomotion, part 1: Basic concepts and terminology*, 1997.

2. Polhemus. *Polhemus G4 Product brochure*.

3. Daniel Broyles, Kyle Kauffman, John Raquet, and Piotr Smagowski. *Non-gnss smartphone pedestrian navigation using barometric elevation and digital map-matching*, 2018.

4. Oleg Mezentsev, Gerard Lachapelle, and Jussi Collin. *Pedestrian Dead Reckoning - A Solution to Navigation in GPS Signal Degraded Areas?* Tampere, Finland, 2005.

5. T.J. Brand and R.E. Phillips. *Foot-to-Foot Range Measurement as an Aid to Personal Navigation*, 2003.

6. Michel Laverne, Michael George, Dale Lord, Alonzo Kelly, and Tamal Mukherjee. *Experimental Validation of Foot to Foot Range Measurements in Pedestrian Tracking*. Portland, OR, 9 2011.

7. Xiaofang Li, Yuliang Mao, Ling Xie, Jiabin Chen, and Chunlei Song. *Applications of zero-velocity detector and Kalman filter in zero velocity update for inertial navigation system*, 2015.

8. Eric Foxlin. *Pedestrian Tracking with Shoe-Mounted Inertial Sensors*, 2005.

9. D. H. (David H.) Titterton and J. L. (John L.) Weston. *Strapdown Inertial Navigation Technology*, 2004.

10. Aaron Canciani. *Integration of Cold Atom Interferometry INS With Other Sensors*. Wright-Patterson Air Force base, Ohio, 2012.

11. Daniel T Johnson. *Combined Stereo Vision and Inertial Navigation for Automated Aerial Refueling*. Wright-Patterson Air Force Base, Ohio, 2017.

12. Micheal J. Veth. *Fusion of Imaging and Inertial Sensors for Navigation*. Wright-Patterson Air Force Base, Ohio, 2006.

13. Warren S. Flenniken IV, John H. Wall, and David M. Bevly. *Characterization of various IMU error sources and the effect on navigation performance*, 2005.

14. Jonathan M Neu. *A Tightly-Coupled INS/GPS Integration Using a MEMS IMU*. Wright-Patterson Air Force Base, Ohio, 2004.

15. Peter S Maybeck. *Stochastic models, estimation, and control Volume 1*, 1979.

16. Peter S. Maybeck. *Stochastic models, estimation, and control. Volume 2*, 1982.

17. Robert Grover Brown and Patrick Y.C. Hwang. *Intro to Random Signals and Applied Kalman Filters*, 1997.

18. Rui Zhang, Hai Yang, Fabian Höflinger, and Leonhard M. Reindl. *Adaptive Zero Velocity Update Based on Velocity Classification for Pedestrian Tracking*, 2017.

19. Khairi Abdulrahim, Terry Moore, Chris Hide, and Chris Hill. *Understanding the Performance of Zero Velocity Updates in MEMS-based Pedestrian Navigation*, 2014.

20. Peter Strömbäck, Jouni Rantakokko, Sven Lennart Wirkander, Mikael Alexandersson, Karina Fors, Isaac Skog, and Peter Händel. *Foot-mounted inertial navigation and cooperative sensor fusion for indoor positioning*, 2010.

21. Zhenwei Li, Chunlei Song, Jingyi Cai, Rui Hua, and Pei Yu. *An Improved Pedestrian Navigation System Using IMU and Magnetometer*, 2017.

22. Chao Li, Jinjun Zheng, Zhuqing Jiang, Xinmeng Liu, Yuying Yang, and Beihang Zhang. *A Novel Fuzzy Pedestrian Dead Reckoning System for Indoor Positioning Using Smartphone*, 2015.

23. Qu Wang, Langlang Ye, Haiyong Luo, Aidong Men, Fang Zhao, and Changhai Ou. *Pedestrian walking distance estimation based on smartphone mode recognition*, 2019.

24. Marzieh Jalal Abadi, Luca Luceri, Mahbub Hassan, Chun Tung Chou, and Monica Nicoli. *A cooperative machine learning approach for pedestrian navigation in indoor IoT*, 2019.

25. Jouni Rantakokko, Peter Strömbäck, and Peter Andersson. *Foot-And knee-mounted INS for firefighter localization*, 2014.

26. Chandra Tjhai and Kyle O'Keefe. *Using step size and lower limb segment orientation from multiple low-cost wearable inertial/magnetic sensors for pedestrian navigation*, 7 2019.

27. Min Su Lee, Hojin Ju, Jin Woo Song, and Chan Gook Park. *Kinematic model-based pedestrian dead reckoning for heading correction and lower body motion tracking*, 11 2015.

28. Kyle Kauffman, Daniel Marietta, John Raquet, Daniel Carson, Robert C. Leishman, Aaron Canciani, Adam Schofield, and Michael Caporellie. *Scorpion: A Modular Sensor Fusion Approach for Complementary Navigation Sensors*, 2020.

29. Daniel T. Johnson, Scott L. Nykl, and John F. Raquet. *Combining stereo vision and inertial navigation for automated aerial refueling*, 2017.

30. A R Jiménez, F Seco, C Prieto, and J Guevara. *A Comparison of Pedestrian Dead-Reckoning Algorithms using a Low-Cost MEMS IMU*, 2009.

31. Inc Analog Devices. *ADIS16470 Data sheet.*

32. Kyle Lethander and Clark Taylor. *Characterization of Analog Devices IMUs.* Wright Patterson Air Force Base.

33. Polhemus. Polhemus is the premier precision motion tracking company. https://polhemus.com/, 2015.

34. Polhemus. *G4 USER MANUAL URM10PH238 JULY 2013 Rev. D*, 2013.

35. Brandon Wagstaff, Valentin Peretroukhin, and Jonathan Kelly. *Robust Data-Driven Zero-Velocity Detection for Foot-Mounted Inertial Navigation*, 2020.

36. Alessio Martinelli, Simone Morosi, and Enrico Del Re. *Daily Living Movement Recognition for Pedestrian Dead Reckoning Applications*, 2016.

Acronyms

AFIT Air Force Institute of Technology. 3, 30, 69

DCM Direction Cosine Matrix. 9, 10, 14, 15, 16

ECEF Earth-Centered Earth-fixed. ix, 9

EKF Extended Kalman Filter. 6, 20, 23, 31, 33

ENU East, North, and Up. ix, 8, 9, 10

GNSS Global Navigation Satellite System. v, 4

GPS Global Positioning System. 1, 3, 30, 47, 48, 52

IMU Inertial Measurement Unit. iv, ix, x, xi, 3, 4, 5, 11, 13, 21, 26, 27, 28, 29, 30, 32, 33, 34, 35, 36, 37, 40, 41, 42, 48, 49, 50, 52, 54, 55, 56, 57, 58, 59, 60, 61, 62, 63, 64, 65, 66, 67, 68, 69, 70

INS Inertial Navigation System. 11

KF Kalman Filter. 6, 11, 20, 21, 22, 23, 24, 25, 30, 34

MEMS Micro-electromechanical Systems. 11, 40

NED North, East and Down. x, 7, 8, 10, 12, 15, 31, 32, 33, 61, 62

PDR Pedestrian Dead Reckoning. iv, v, ix, x, xi, 1, 2, 3, 4, 5, 6, 25, 26, 27, 28, 29, 30, 31, 33, 34, 40, 45, 46, 48, 50, 52, 54, 55, 56, 57, 58, 59, 60, 61, 62, 63, 64, 65, 66, 67, 68, 69, 70

STK Scorpion Development Toolkit. v, xi, 29, 30, 33, 34, 35, 55, 56, 66, 69

SWaP Size, Weight, and Power. 2

WGN White Gaussian Noise. 21, 23, 41

WGS-84 World Geodetic System of 1984. 7

ZUPT Zero Velocity Update. iv, x, 2, 4, 25, 26, 29, 30, 33, 34, 35, 36, 52, 56, 61, 62, 63, 64, 66, 68, 69

REPORT DOCUMENTATION PAGE

Form Approved
OMB No. 0704–0188

1. REPORT DATE *(DD–MM–YYYY)*	2. REPORT TYPE	3. DATES COVERED *(From — To)*
25–03–2021	Master's Thesis	Sept 2019 — Mar 2021

4. TITLE AND SUBTITLE

Development of a Testbed for Foot Mounted based Pedestrian Dead Reckoning(PDR) systems

5a. CONTRACT NUMBER

5b. GRANT NUMBER

5c. PROGRAM ELEMENT NUMBER

6. AUTHOR(S)

Eldridge, Jordan, Capt, USAF

5d. PROJECT NUMBER

5e. TASK NUMBER

5f. WORK UNIT NUMBER

7. PERFORMING ORGANIZATION NAME(S) AND ADDRESS(ES)

Air Force Institute of Technology
Graduate School of Engineering and Management (AFIT/EN)
2950 Hobson Way
WPAFB OH 45433-7765

8. PERFORMING ORGANIZATION REPORT NUMBER

AFIT-ENG-MS-21-M-032

9. SPONSORING / MONITORING AGENCY NAME(S) AND ADDRESS(ES)

Intentionally Left Blank

10. SPONSOR/MONITOR'S ACRONYM(S)

11. SPONSOR/MONITOR'S REPORT NUMBER(S)

12. DISTRIBUTION / AVAILABILITY STATEMENT

DISTRIBUTION STATEMENT A:
APPROVED FOR PUBLIC RELEASE; DISTRIBUTION UNLIMITED.

13. SUPPLEMENTARY NOTES

14. ABSTRACT

Over the last several years of research into the field of Pedestrian Dead Reckoning (PDR), there have been varying degrees of success in providing a viable individual navigation system. The PDR solutions developed utilize everything from a single Inertial Measurement Units (IMU) to several IMUs with additional sensors. One specific PDR solution identified that by utilizing a micro-mechanical Inertial Measurement Unit (IMU) on each foot (along with the application of Zero Velocity Updates (ZUPT) and foot-to-foot range measurements) a reliable method of PDR tracking could be accomplished. Their study concludes that further evaluation is required for this foot-mounted solution to be viable as a wearable PDR system. In order to better deliver a viable wearable system, this research focuses on the development of a PDR testbed that can be utilized to evaluates a variety of sensors and techniques.

15. SUBJECT TERMS

Pedestrian Dead Reckoning (PDR), Extended Kalman Filter (EKF), Inertial Navigation, Pedestrian Navigation

16. SECURITY CLASSIFICATION OF:			17. LIMITATION OF ABSTRACT	18. NUMBER OF PAGES	19a. NAME OF RESPONSIBLE PERSON
a. REPORT	b. ABSTRACT	c. THIS PAGE			Dr. Clark Taylor, AFIT/ENG
U	U	U	UU	89	19b. TELEPHONE NUMBER *(include area code)* (937) 255-3636 x9999; Clark.Taylor@afit.edu